HAL
open science

Microcanonical multifractal formalism–a geometrical approach to multifractal systems: Part I. Singularity analysis

Antonio Turiel, Hussein Yahia, Conrad J. Perez-Vicente

To cite this version:

Antonio Turiel, Hussein Yahia, Conrad J. Perez-Vicente. Microcanonical multifractal formalism–a geometrical approach to multifractal systems: Part I. Singularity analysis. Journal of Physics A: Mathematical and Theoretical, 2008, Journal of Physics A: Mathematical and Theoretical, 41, pp.015501-015536. 10.1088/1751-8113/41/1/015501 . hal-00937370

HAL Id: hal-00937370

https://inria.hal.science/hal-00937370v1

Submitted on 28 Jan 2014

HAL is a multi-disciplinary open access archive for the deposit and dissemination of scientific research documents, whether they are published or not. The documents may come from teaching and research institutions in France or abroad, or from public or private research centers.

L'archive ouverte pluridisciplinaire **HAL**, est destinée au dépôt et à la diffusion de documents scientifiques de niveau recherche, publiés ou non, émanant des établissements d'enseignement et de recherche français ou étrangers, des laboratoires publics ou privés.

IOP PUBLISHING JOURNAL OF PHYSICS A: MATHEMATICAL AND THEORETICAL

J. Phys. A: Math. Theor. **41** (2008) 015501 (35pp) doi:10.1088/1751-8113/41/1/015501

Microcanonical multifractal formalism—a geometrical approach to multifractal systems: Part I. Singularity analysis

Antonio Turiel[1], **Hussein Yahia**[2] **and Conrad J Pérez-Vicente**[3]

[1] Institut de Ciències del Mar—CSIC. Passeig Marítim de la Barceloneta, 37-49, 08003 Barcelona, Spain
[2] Clime Project. INRIA Roquencourt, Domaine de Voluceau, B.P. 105, 78153 Le Chesnay Cedex, France
[3] Departament de Fisica Fonamental, Universitat de Barcelona, Diagonal, 647, Barcelona 08028, Spain

Received 18 June 2007, in final form 6 November 2007
Published 12 December 2007
Online at stacks.iop.org/JPhysA/41/015501

Abstract
Multifractal formalism in the microcanonical framework has proved to be a valuable approach to understand and analyze complex signals, typically associated with natural phenomena in scale invariant systems. In this paper, we discuss the multifractal microcanonical formalism in a comprehensive, unified way, including new theoretical proofs and validation tests on real signals, so completing some known gaps in the foundations of this theory. We also review the latest advances and describe the present perspectives in this field. Some technical details on the implementation of involved algorithms and relevant open issues are also discussed.

PACS numbers: 47.53.+n, 89.75.Da, 47.11.+j

1. Introduction

Systems displaying scale invariant behavior have been frequently reported in the physics literature since the early days of statistical mechanics [1]. The prototype of a scale-invariant phenomenon is a phase transition [2–4]. In a first-order phase transition there is an abrupt change in one or more properties of a physical system; in higher order transitions, different thermodynamic observables as well as some time and spatial correlation functions display power-law behavior. The phenomenon can be considered as a fingerprint of scale invariance. A proper, full characterization of a critical point requires the determination of the scaling exponent: it was soon realized that systems characterized by the same values of the singularity exponents formed a particular universality class: close to the critical point, the details on the microscopical dynamics of the system become irrelevant and the macroscopic features of the class are precisely determined by the exponents [2]. Thus, it makes sense to classify

physical systems according to the values of the set of critical exponents since it is a manner to gain insight on the behavior of complex systems from their simplest representatives in the respective universality class.

Fractal sets are reasonable candidates for the realization of critical manifolds (extending the concept of critical points) in dynamical systems since attractor sets are, in many cases, fractal. Fractal sets have an intrinsic scale invariant nature due to their origin which can be expressed by a characteristic exponent that is the fractal dimension of the set. For a homogeneous fractal F, with fractal dimension D_F, many relevant scale-dependent quantities (e.g., spatial correlation between points in F, probability of intercepting F with balls of radius $\mathbf{r}$, etc) decay as a power law of the scale $\mathbf{r}$ with exponents which are directly related to the fractal dimension D_F [5]. The widespread occurrence of this behavior led researchers to interpret those systems in terms of fractal sets, and try to characterize universality classes in terms of possible underlying fractal attractors or fractal interfaces [2].

Nevertheless, a better understanding of the mechanisms that govern the evolution of some dynamical systems, turbulent flows being one of the most relevant cases, evidences that the observed intrinsic complexity could not be covered by a simple description based on the existence of a single fractal interface. As a consequence, a richer framework was required and the natural step forward was to consider multiple-fractal hierarchies which could fit better with the available evidence. Bi-fractal, first, and soon multifractal characterizations of such systems were applied to fit experimental data. In a celebrated paper, Parisi and Frisch [6] put into evidence the connection between an underlying multifractal hierarchy and the spectrum of exponents observed in the structure functions obtained from a turbulent flow in the regime of fully developed turbulence (FDT). Hence, the different fractal components in a multifractal system are conveniently arranged to give as a result the observed scaling exponents [7]. The interest on multifractals considerably grew, giving rise to many papers devoted to assess the presence of a multifractal hierarchy in physical systems, and then to exploit this fact to characterize them from a statistical point of view ([8] and the references herein).

The standard approach studies multifractal using global statistical descriptors applied to the system under study. Thus, the hierarchy of scaling exponents is derived by the analysis of averaged statistical observables (e.g., structure functions, which are identified with the moments of order p of an intensive variable that depends on a scale scope $\mathbf{r}$). In order to evaluate the observables, the system is required to have stationary averages (i.e., the average over a single realization large enough is close to the average over different realizations). In FDT, stationarity of the moments is necessary to obtain structure functions and this can be done by averaging over different spatial locations of the same flow realization. In such an instance, we speak about the canonical multifractal framework: we do not identify individual states (the fractal components), but the 'thermalized averages' (that is, averages over the fractal components) of some variables. The multifractal hierarchy is assessed indirectly, by observing the scaling behavior of these averages. The canonical multifractal framework has been widely employed since its introduction, and even nowadays it is the most common approach in the experimental study of multifractal systems.

An alternative to the global approach is a microscopical, geometrical approach, in which the different fractal components are isolated in each single realization of a physical system. This is the basic goal of the microcanonical multifractal framework: to isolate and identify the individual fractal microstates. Separating the fractal components is computationally much harder than computing canonical averages, as it requires greater accuracy and the resolution of some practical processing issues. Thanks to the application of the microcanonical multifractal framework, new processing tools are now available, and only within this scenario the dynamics of some multifractals systems can be properly understood.

This paper intends to be a review of the basic concepts and tools for the application of the microcanonical multifractal framework. We will explain in detail the theoretical foundations of the formalism and how to apply these concepts in practical situations. In section 2, we set up some conventions used throughout the paper. Section 3 gives a general introduction to the canonical framework and also addresses its relation with multiplicative processes and energy cascades. Microcanonical multifractality is introduced in section 4. We start by considering multiaffine signals and then, we introduce the general notion of multifractal measure as well as the fundamental concept of multifractal decomposition. These ideas are illustrated through some examples. In section 5, the connection with the energy cascade is developed to justify the accurate reconstruction of a turbulent signal from its most singular component (MSC). The theoretical setting and the algorithms are presented in depth as they help to understand the concept of reduced signal which is of fundamental importance for the study of geophysical flows and turbulent signals (the reduced signal is presented in the second part of this paper). Finally, our conclusions are outlined in section 6.

2. Settings and conventions: data

2.1. Settings and conventions

The notation $o(r^\alpha)$ means a quantity which becomes negligible in comparison with r^α as r goes to zero, namely

$$\lim_{r\to 0} \frac{o(r^\alpha)}{r^\alpha} = 0. \tag{1}$$

Throughout the paper, we will denote a signal by $s(\mathbf{x})$, where $\mathbf{x}$ stands for the position vector in a d-dimensional real space $\mathbb{R}^d$. In general, signals will only be defined over a compact domain $\Omega \subset \mathbb{R}^d$. The symbol $*$ denotes the convolution product that will be extended to the convolution dot product for vector-valued functions; namely, if $\mathbf{v}(\mathbf{x}) = (v_i(\mathbf{x}))$ and $\mathbf{u}(\mathbf{x}) = (u_i(\mathbf{x}))(1 \leqslant i \leqslant d)$ are two vector-valued functions, their convolution dot product $(\mathbf{v} * \mathbf{u})(\mathbf{x})$ is given by

$$(\mathbf{v} * \mathbf{u})(\mathbf{x}) = \mathbf{Tr}((v_i * u_j)(\mathbf{x})) = \sum_{i=1}^{d} (v_i * u_i)(\mathbf{x}). \tag{2}$$

The Fourier transform of a function $s(\mathbf{x})$ will be denoted by $\hat{s}(\mathbf{f})$, where $\mathbf{f}$ is defined in the frequency space. The power spectrum of the signal, $S(\mathbf{f})$, is defined as

$$S(\mathbf{f}) = \langle |\hat{s}|^2(\mathbf{f})\rangle \tag{3}$$

where the average $\langle\cdot\rangle$ is taken over the ensemble of signals s under study. With this definition, the power spectrum is the Fourier transform of the averaged autocorrelation of the signal s, which coincides with the two-point correlation of the ensemble of signals when the ensemble is statistically translationally invariant [9–11]. The power spectrum is a quantity that has been widely used to make the link between geometry and statistics, and to determine if a system possess statistical scale invariance. Many signals are observed to possess a power spectra scaling as

$$S(\mathbf{f}) \approx A_0\, \mathbf{f}^{-(2-\eta)} \tag{4}$$

where the deviation exponent η can take a broad range of values. Thus, for FDT $\eta = 1/3$ (the famous 5/3 law, [12]), while for natural images η takes a small value which depends on the particular ensemble under analysis [13–15]. The reference value -2 in the exponent implies a high-degree of non-stationarity in the signal, typical of piecewise continuous functions [16].

Such non-stationarity is present in signals of very different nature such as natural images [13, 14], econometric time series [15, 17], DNA sequences [18] and geophysical signals of different types [16]. For all those signals, a good strategy to recover stationarity is to define a signal s' obtained by taking derivatives or increments on s. Note that differentiating a signal is read in the Fourier space as multiplying it by $i\mathbf{f}$. According to the definition of the power spectrum, equation (3), the power spectrum $S'(\mathbf{f})$ associated with s' is then $S'(\mathbf{f}) = f^2 S(\mathbf{f}), \approx A_0$ for $\eta = 0$, so it is constant. Constant spectra mean total spatial decorrelation and, hence, the signal is stationary. Not surprisingly, one of the first strategies to analyze the local behavior of a signal is to take increments around any point under study.

Another concept which will be relevant in the course of this paper concerns the wavelet transform of the signal [19, 20]. Given a wavelet $\Psi(\mathbf{x})$, we define the wavelet projection (or wavelet transform) of a signal s at the point $\mathbf{x}$ and the scale r, denoted by $T_\Psi s(\mathbf{x}, r)$, as

$$T_\Psi s(\mathbf{x}, r) = \frac{1}{r^d} \int s(\mathbf{y})\, \Psi\left(\frac{\mathbf{x}-\mathbf{y}}{r}\right) \mathrm{d}\mathbf{y} = s * \Psi_r(\mathbf{x}) \tag{5}$$

where $\Psi_r(\mathbf{x}) = \dfrac{1}{r^d}\Psi\left(\dfrac{\mathbf{x}}{r}\right)$. We want to point out here that when wavelet projections are used for signal analysis, it is not required, in general, that Ψ verifies the admissibility condition

$$\int \frac{|\hat{\Psi}|^2(\mathbf{f})}{|f_1| \cdots |f_d|}\, \mathrm{d}\mathbf{f} < \infty, \tag{6}$$

which is only necessary to recover the function s from the values of its wavelet projections [19]. As a matter of fact, our interest in wavelets concerns their capability of producing smooth interpolations among scales as well as of localizing characteristic structures at any scale. In addition, they are useful to filter noise and long-range correlations. In this paper, we will consider two families of wavelets: Gaussian and Lorentzian. The basic Gaussian wavelet $G(\mathbf{x})$, is given by

$$G(\mathbf{x}) = \exp\left(-\tfrac{1}{2}\|\mathbf{x}\|^2\right). \tag{7}$$

The β-Lorentzian wavelet $L_\beta(\mathbf{x})$ is given by

$$L_\beta(\mathbf{x}) = \frac{1}{(1+\|\mathbf{x}\|^2)^\beta}. \tag{8}$$

Note that both types of wavelets are isotropic, that is, they do not privilege any particular direction. The functions G and L_β are positive so that they are not admissible wavelets. However, for some of the tests we will need to use the derivative of positive functions as analysis wavelets. For those cases, we have used the nth-order isotropic derivatives of the Gaussian and β-Lorentzians. We define the nth-order isotropic derivative of a function $F(\mathbf{x})$ as the function $F^n(\mathbf{x})$ which verifies

$$\hat{F}^n(\mathbf{f}) = \|\mathbf{f}\|^n\, \hat{F}(\mathbf{f}). \tag{9}$$

To keep notation simple, we will denote the nth-order isotropic derivative of G and L_β by G^n and L^n_β, respectively, and they will be referred to as the nth-order Gaussian and the nth-order β-Lorentzian.

2.2. Data

For illustration purposes, we have considered throughout the paper two different signals which exhibit multifractal properties.

The first one is a 2D-domain signal: a satellite image, acquired by the MeteoSat satellite in the thermal infrared spectral range, in an area over Western Equatorial Africa. This type of

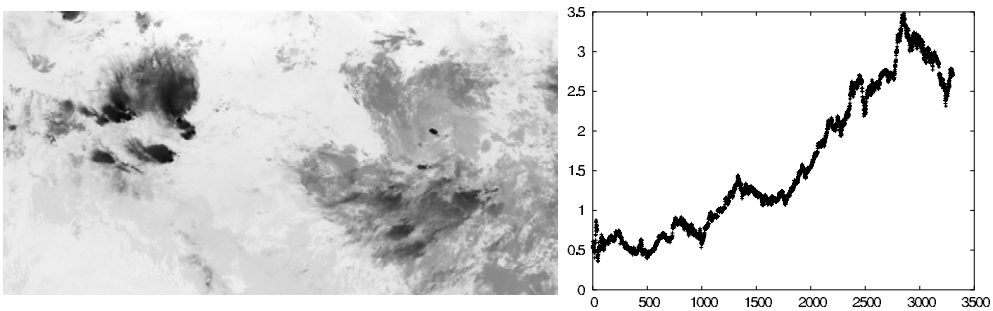

Figure 1. Left: MeteoSat thermal infrared image, acquired at 00:00 GMT on 31 July 1998. The area shown goes from 0 to 40° east, and from 0 to 20° north. Right: Series of the logarithm of the daily quotation prices (in euros) for Telefónica™ stock between 1990 and 2000; the x axis is given in market days since 1 January 1990.

images is used to assess the temperature of the higher layers of the atmosphere. The atmosphere can be seen as a stratified flow, except at locations and scales where convection predominates [21] and, in both cases, FDT is present, either in the form of 2D or 3D turbulence. As a consequence, temperature should have a multifractal structure, consequence of the advective forcing of the turbulent flow [12]. Meteosat infrared images, as that shown in figure 1, left, have been checked to possess multifractal structure [21, 22].

The second signal has 1D domain: it stands for the daily quotation price of a highly capitalized Spanish stock market asset, Telefónica™, for a period of about 10 years. It is well known that the absolute value of returns (i.e., relative variations of the price over a given period) of stock market prices are power-law correlated in time [15, 17], what has been interpreted as an evidence of the scale-invariant character of the stock market evolution. Such an evolution would be an emergent property in a complex system consisting of a large ensemble of interacting agents with different information, capital and strategies. This type of signals has also been reported as multifractal [23–25]. This 1D signal is shown in figure 1, right.

3. Canonical approach to multifractality

3.1. General considerations

In this section, we present some basic theoretical aspects about the canonical framework, to make clearer its connection and differences with the microcanonical approach. We do not pretend, however, to perform an exhaustive review on this subject since it has been thoroughly discussed in the scientific literature [8, 26]. From a technical point of view let us mention [27–30] as references about the theoretical limitations of the formalism and ways to overcome them, and [26, 31–34] about practical implementations. Besides, we do not present any test on the applicability of the canonical formalism to real data. Rather, we directly refer to many studies reporting multifractality in a canonical way in different contexts such as econophysics [23, 35], natural images [36, 37], different geophysical signals [16] and even heart-beat dynamics [38, 39], to cite some examples, although the most studied physical system is FDT (let us cite [40] as a possible consensus reference). In fact, the first theoretical explanation aimed at supporting the empirical observation of multifractality in a canonical way in FDT was given by Kolmogorov in one of his famous 1941 papers [41].

In a canonical approach, multifractality is observed when the probability distribution of some particular scale-dependent intensive variables follow a power-law behavior. In a more formal way, for a given signal $s(\mathbf{x})$ there exists at least one scale-dependent local functional $\mathbb{T}_r$ which defines the function $\mathbb{T}_r s(\mathbf{x})$ with the desired properties. The function $\mathbb{T}_r s(\mathbf{x})$ depends on the basis point $\mathbf{x}$ and the scale parameter r where r determines the degree of locality of the functional $\mathbb{T}_r$. Typical examples of $\mathbb{T}_r$ are wavelet transforms at scale r or some differential operators applied to the signal. The valid shape of the functional must be checked in each context. To be more precise, we will say that a signal is (canonically) multifractal if, for a given family of functionals $\mathbb{T}_r$, we have locally when $r \to 0$:

$$\langle |\mathbb{T}_r \mathbf{s}|^p \rangle = \alpha_p \, r^{\tau_p} + o(r^{\tau_p}) \tag{10}$$

where the average $\langle \cdot \rangle$ is taken over the ensemble of signals s belongs to (the coefficient α_p depends on the functional $\mathbb{T}_r$). In practice, such an ensemble average is not accessible and what is actually computed is an average over different points $\mathbf{x}$ in the same realization s. In the literature on turbulence it is usual to call each of the quantities $\langle |\mathbb{T}_r \mathbf{s}|^p \rangle$ the order p structure function and the functional $\mathbb{T}_r s$ usually stands for the difference of velocities between two points a distance r apart or the local dissipation of energy on a ball of radius r.

3.2. Multiplicative processes

Kolmogorov had the intuition that in FDT energy is transmitted from the large-scale structures (eddies) to the smaller ones by a simple mechanical transfer process, and therefore, when the fluid attains a state of 'dynamical equilibrium' we should expect a balance in the amount of energy stored in each scale. Kolmogorov proposed the following: given two scales r and l, $0 < r < l$, one can characterize their distributions by means of an injection parameter $\eta_{r/l}$ such that

$$|\mathbb{T}_r s| \doteq \eta_{r/l} \, |\mathbb{T}_l s| \tag{11}$$

where the symbol '$\doteq$' means that both sides are equally distributed. Note that we do not claim that $|\mathbb{T}_r s(\mathbf{x})| = \eta_{r/l} \, |\mathbb{T}_l s(\mathbf{x})|$ for all $\mathbf{x}$, which would be a very strong requirement and could only be verified for a very particular, well-chosen class of functionals, depending on the signal [42, 43]. Kolmogorov stated that the injection $\eta_{r/l}$ only depends on the ratio of scales, $\eta_{r/l} = (r/l)^\delta$. Taking moments at both sides of equation (11) and then averaging, we obtain

$$\langle |\mathbb{T}_r \mathbf{s}|^p \rangle = \left(\frac{r}{l}\right)^{\delta p} \langle |\mathbb{T}_l \mathbf{s}|^p \rangle = A_p \, r^{\delta p} \tag{12}$$

where $A_p = \langle |\mathbb{T}_l \mathbf{s}|^p \rangle \rangle l^{-\delta p}$. From equation (10) it follows that $\tau_p = \delta p$, that is, the canonical exponents τ_p depend linearly on p. It has been verified [12] that an injection mechanism as the one proposed by Kolmogorov leads to a geometrical arrangement of contributing points which has non-trivial fractal dimension D, which can be deduced from the injection exponent δ. The precise relation between D and δ depends on the particular functional used and, for instance, for the local energy dissipation one gets $\delta = D - d < 0$ [12].

A linear scaling in the canonic exponents τ_p is referred to as 'normal scaling' and the system is monofractal. However, experiments in FDT show that the scaling is not linear with p; rather, it is a convex curve. Such a behavior is referred to as 'anomalous scaling' and the associated systems are usually called multifractal. As a matter of fact, anomalous scalings are the most frequent cases. Any curve τ_p can be approximated by linear segments, each one representing a different fractal component. Thus, to obtain the smooth, nonlinear curves τ_p coming from experiments, it would be necessary to have an infinite collection of fractals, forming the so-called multifractal hierarchy. All these intuitive ideas can be formalized in a

more precise way, but we prefer to defer this specific discussion to section 4.1, in which the link between the geometrical arrangement of fractal components and the canonical exponents τ_p will be made explicit.

It is obvious that the assumption of considering $\eta_{r/l}$ as a constant injection parameter fails for those cases in which anomalous scaling is observed. However, equation (11) can be generalized to account for anomalous scalings provided $\eta_{r/l}$ is a random variable, it only depends on the ratio r/l and it is independent of $\mathbb{T}_l s$. We proceed as follows: let us suppose that we have defined a variable $\mathbb{T}_r s$ for which multifractality in a canonical sense, equation (10), is observed. Thus, given two scales r and l (we drop the correction terms to alleviate notation) we obtain

$$\frac{\langle|\mathbb{T}_r \mathbf{s}|^p\rangle}{\langle|\mathbb{T}_l \mathbf{s}|^p\rangle} = \left(\frac{r}{l}\right)^{\tau_p}. \tag{13}$$

Let us now suppose that for any $0 < k < 1$ there exists a random variable η_k such that $\langle\eta_k^p\rangle = k^{\tau_p}$. Two conditions must be verified to construct η_k. First, the expressions k^{τ_p} must be valid p-moments of a positive variable. This implies that the curve τ_p versus p must be convex, due to Jensen's inequality [44] applied to the moments. Note that if τ_p are canonical exponents obtained from equation (10) they necessarily form a convex curve. The second requirement is that the moments $\langle\eta_k^p\rangle$ must contain enough information to retrieve the probability distribution [45]. This is the moment problem, studied since Carleman [46]: there is a unique solution provided τ_p does not diverge too fast with p. Once the variable η_k is constructed, we have

$$\langle|\mathbb{T}_r \mathbf{s}|^p\rangle = \langle\eta_{r/l}^p\rangle\langle|\mathbb{T}_l \mathbf{s}|^p\rangle. \tag{14}$$

If the structure functions $\langle|\mathbb{T}_r \mathbf{s}|^p\rangle$ and $\langle|\mathbb{T}_l \mathbf{s}|^p\rangle$ do not diverge too fast with p, we can apply the equation given above to reconstruct the distributions of the variables $\mathbb{T}_r s$ and $\mathbb{T}_l s$. We obtain as a consequence equation (11), but now $\eta_{r/l}$ is a random variable, independent of $|\mathbb{T}_l s|$. If we can define the variable η_k for any k, then for any k, k' we have

$$\eta_k\, \eta_{k'} \doteq \eta_{kk'} \tag{15}$$

what in terms of the variables $\mathbb{T}_r s$ gives rise to the known 'energy cascade': for any scales $r < l$ we have that the energy transfer from the scale l to the scale r can be either verified directly or passing through any intermediate scale r'. As we can decompose the process in any number of intermediate stages, it follows that the distribution for the variables η_k must be infinitely divisible [47] with respect to the parameter k, that is, equation (15) is verified. The class of infinitely divisible processes is quite broad and includes particular processes which are discrete in scale [48] although we will be interested, in general, in processes which are continuous in scale [49, 50], as they can be considered as more physically sound.

The existence of the cascade implies that the process relating the variables $\mathbb{T}_r s$ at different scales can be hierarchically organized: the energy enters the system at the greater scales, then it propagates down the cascade up to smallest scales, where it is dissipated. The existence of an energy cascade has been always considered as an important feature of turbulent systems, as it shows that the coherent, large-scale modes of motion are progressively degraded to shorter-ranged movements which eventually degrade to heat, which is a manifestation of disordered (molecular) motion. The hierarchy is established taking into account that the leading motion modes (those at the larger scales) organize all the fluid, because from them we can deduce (at least, statistically) how all the other modes are organized. We will see in section 5 that the existence of the cascade can be interpreted in explicit geometric terms in the microcanonical formulation.

4. Microcanonical approach to multifractality

4.1. Generalities

Multifractality in a microcanonical sense is observed if there exists local power-law scaling behavior for each point in the signal domain. Given a signal $s(\mathbf{x})$, it is processed by a scale-dependent local functional $\mathbb{T}_r$ to obtain the function $\mathbb{T}_r s(\mathbf{x})$, that depends on the basis point $\mathbf{x}$ and the scale parameter r and that determines the degree of locality of the functional $\mathbb{T}_r$. We will say that a signal is multifractal in a microcanonical sense if, for at least one functional $\mathbb{T}_r$, the following relation holds for any point $\mathbf{x}$ on a dense set of $\mathbb{R}^d$.[4]

$$\mathbb{T}_r s(\mathbf{x}) = \alpha(\mathbf{x})\, r^{h(\mathbf{x})} + o(r^{h(\mathbf{x})})(r \to 0) \tag{16}$$

for some functions $\alpha(\mathbf{x})$ and $h(\mathbf{x})$. Although the multiplicative term $\alpha(\mathbf{x})$ depends on the particular functional $\mathbb{T}_r$ chosen, the exponent $h(\mathbf{x})$ should be independent of it. Note that for small scales r (such that the $o(r^{h(\mathbf{x})})$ term becomes negligible) all the dependence on the scale parameter is concentrated in the factor $r^{h(\mathbf{x})}$, and thus the knowledge of the exponent $h(\mathbf{x})$ allows us to interpret the degree of regularity of the function at $\mathbf{x}$. For that reason, it is a common convention to call these exponents 'singularity exponents' of the multifractal. By classifying all the points sharing the same singularity exponent, we obtain the so-called transition fronts or singularity components of the system. We denote by $\mathcal{F}_h$ the singularity component associated with the singularity value h, and it is defined as follows:

$$\mathcal{F}_h = \{\mathbf{x} : h(\mathbf{x}) = h\}. \tag{17}$$

A geometrical arrangement of the points satisfying equation (16) not only has been experimentally observed in very different signals [22, 43, 51, 52] (see also subsection 4.2.1), in some instances it can also be theoretically predicted using a simple, purely geometric argument. From a classical theorem in the theory of weakly differentiable functions ([20], theorem 2.7) the total variation of s, whenever finite, is the integral of the 1-dimensional Hausdorff measure of the level-sets of s. Consequently, a power-law behavior of the type described by equation (16) should be expected for those points which contribute to the divergence of the total variation integral. As we will see in section 4.2.2, the basic functional used in the microcanonical multifractal formalism is the integral of the signal gradient (maybe understood in a distributional sense), what confirms the relevance of this geometric argument.

It is important to remark that to properly talk about a multifractal signal, we cannot only require equation (16) to hold. We should also require the singularity components to be hierarchically arranged as a network of sets with different fractal dimensions. Let us suppose that the singularity component $\mathcal{F}_h$ has fractal dimension $D(h)$. The function $D(h)$ is known as the *singularity spectrum* of the multifractal. According to Parisi and Frisch's derivation [6], the canonical exponents τ_p, associated with the structure functions of order p, are related to the singularity spectrum $D(h)$ through

$$\tau_p = \inf_h\{ph + d - D(h)\} \tag{18}$$

where, as before, d is the dimension of the embedding space. Thus, the step from fractal geometry of the system to its global statistical properties is mediated by the singularity components since equation (18) shows that the canonical exponents are given by the Legendre transform of the singularity spectrum. By construction, the Legendre transform of a function is convex. Conversely, if $D(h)$ is also convex, the singularity spectrum can be retrieved from the canonical exponents by applying again a Legendre transform

$$D(h) = \inf_p\{ph + d - \tau_p\}. \tag{19}$$

[4] For the remaining of this paper, any functional equality should be understood to hold on a dense set of $\mathbb{R}^d$.

This estimate of the singularity spectrum is known as the Legendre spectrum. Many methods based on the multifractal canonical formalism rely on equation (19) to evaluate the singularity spectrum from the indirect evidence furnished by the canonical exponents τ_p. A technical detail should be exposed here: the Legendre spectrum may differ from the actual singularity spectrum since in the canonical formalism there is no way to know if the spectrum given by equation (19) is the actual one or just its convex hull. This knowledge is only granted in a microcanonical formulation. In fact, when the microcanonical formalism can be applied, there is a simple way to compute the singularity spectrum. Let us suppose that we evaluate the singularities at a resolution scale r_0 which is small enough. The distribution of singularities at this scale, $\rho_{r_0}(h)$, must verify [5]

$$\rho_{r_0}(h) = A_0 r_0^{d-D(h)} + o\left(r_0^{d-D(h)}\right) \tag{20}$$

which means that the singularity spectrum can be retrieved from the empirical histogram of singularity exponents. One can even go beyond if one further assumes, to simplify the analysis, that there exists a singularity component $\mathcal{F}_{h_1}$ of maximum dimensionality, $D(h_1) = d$. This is not a strong hypothesis in general: if the functional $\mathbb{T}_r s$ has total support at any finite size r, and the signal is not strictly monofractal, such a component must exist [53] (monofractal systems can also be considered with some specific adaptations [54]). Applying such assumption to equation (20), we obtain a good estimate of the singularity spectrum by means of the following formula:

$$D(h) = d - \frac{\log\left(\rho_{r_0}(h)/\rho_{r_0}^M\right)}{\log r_0} \tag{21}$$

where $\rho_{r_0}^M = \max_h\{\rho_{r_0}(h)\}$. Equation (21) is commonly referred to as the 'histogram method' for the evaluation of the singularity spectrum [5, 55, 56].

Due to the limitations of the canonical multifractal formalism, it has been commonly accepted that a system can only be considered as multifractal if the singularity spectrum is convex (and hence, it can be retrieved by means of the Legendre estimate). One of the advantages of the microcanonical multifractal formalism is that it allows us to extend the concept to situations in which the spectrum has more than one maximum. However, for the scope of this paper, and taking into account that this is the most common experimental situation, we will restrict ourselves to the cases of convex singularity spectra. This leads to the following definitions.

Definition (microcanonical multifractal formalism)**.** *A multifractal d-dimensional scalar (real or complex) signal $s(\mathbf{x})$ verifies the following points:*

(i) there exists at least a family of functionals $\{\mathbb{T}_r\}_r$ such that equation (16) holds for any point $\mathbf{x} \in \Omega$;
(ii) at any scale r_0, equation (20) holds for the same curve $D(h)$;
(iii) the singularity spectrum $D(h)$ derived from equation (20) is a convex function of h.

The experimental validation of microcanonical multifractality on a signal will thus proceed in three steps, according to the three points given above. First, equation (16) should be verified with a good accuracy for a large enough range of scales r and for the majority of the points in the signal domain. Second, applying equation (21) at different resolution scales r_0 we should obtain the same curve $D(h)$, so validating the scale invariant character. Finally, $D(h)$ must be convex. To carry out this task there are two different conceptual strategies that we will discuss in the next subsections.

4.2. Processing the signal: multiaffine functions and multifractal measures

There is no canonical way to know *a priori* for which functional $\mathbb{T}_r$ a signal s will be evidenced as multifractal, so the only way is to test some usual definitions. There are two basic functionals which have demonstrated to be useful to this goal. This leads to two ways to deal with multifractal signals in the microcanonical framework, either to analyze them as multiaffine functions or through appropriate multifractal measures. In this subsection we analyze both in detail.

4.2.1. Multiaffine functions. In the context of microcanical multifractality, a signal is said multiaffine [8, 12, 27] if, locally around any point $\mathbf{x} \in \Omega$:

$$|s(\mathbf{x}+\mathbf{r}) - s(\mathbf{x})| = \alpha_l(\mathbf{x})\, \|\mathbf{r}\|^{\gamma(\mathbf{x})} + o(\|\mathbf{r}\|^{\gamma(\mathbf{x})})(r \to 0) \tag{22}$$

Multiaffine functions possess local Hölder exponents $\gamma(\mathbf{x})$ at each point $\mathbf{x}$ characterizing the local degree of regularity (or singularity) of the function at that point [19, 57, 58]. We are assuming here that for almost any possible direction $\mathbf{r}/\|\mathbf{r}\|$ the obtained Hölder exponent is the same (note that in equation (22) $\mathbf{r}$ stands for a position vector, and the corresponding scale is given by $\|\mathbf{r}\|$); note that in general γ will also depend on the direction $\mathbf{r}/\|\mathbf{r}\|$.

There are some considerations affecting multiaffine signals that must be taken into account. The range of values that the singularity exponents $\gamma(\mathbf{x})$ can take is always bounded by below for real physical signals. Real signals cannot diverge to infinity at any point, because this would imply an infinite energy (or matter) expense or supply. Thus, real signals are bounded on compacts subsets in $\mathbb{R}^d$ and hence, for any point $\mathbf{x}$ there exists an upper bound A_0 such that $|s(\mathbf{y})| < A_0\, \forall\, \mathbf{y} \in U_\mathbf{x}$ for a certain open neighborhood $U_\mathbf{x}$ of $\mathbf{x}$. These bounds rely on general physical principles independently of the resolution level at which the signal is described (namely, the number of sampling points). For instance, the temperature of sea water is always below 100° C (of course, even lower), and no point can attain higher temperatures on the Earth. The existence of bounds on the signal implies that the singularities are bounded by below, because $|s(\mathbf{x}+\mathbf{r}) - s(\mathbf{x})| < 2A_0$ and hence $\gamma(\mathbf{x}) \geqslant 0$ at any point $\mathbf{x}$. So, we should expect that the singularity exponents obtained from the analysis of real signals are always above 0. This is in conflict with some models used to describe certain physical phenomena in which unbounded singularities can be allowed in a realization of the signal (e.g. multiplicative cascades of log-Normal or log-Levy stochastic processes) [49, 50, 59].

In practice, few physical signals are multiaffine due to the presence of some extra contributions whose nature is beyond the multifractal paradigm. These extra contributions appear superimposed to the ideal, multifractal signal, and account for long-range correlations [8]. Typically those long-range correlations are differentiable functions $L(\mathbf{x})$ with integer Hölder exponents $H_C(\mathbf{x})$. In fact, except for extrema (which have zero derivative) we can consider that $H_C(\mathbf{x}) = 1$ from the mean-value theorem for differentiable functions. The problem with multiaffine functions arises when the exponent H_C is smaller than some of the exponents associated with the smoothest components in the multifractal hierarchy because, in this case, the dominant contribution comes from the correlation term and part of the multifractal hierarchy is lost. Long-range masking effects of this type include sun glint, solar heating, wind effect on the sea, etc in satellite images and long-range tendencies in time series to cite some examples.

As a consequence, a natural question concerns the design of mechanisms to get rid of those terms masking the pure multifractal structure of a multiaffine signal. It has been commonly accepted that long-range correlations appear as an additive contribution [8, 26]. In such a case, a possible way to filter this type of contribution is to wavelet-transform the signal by

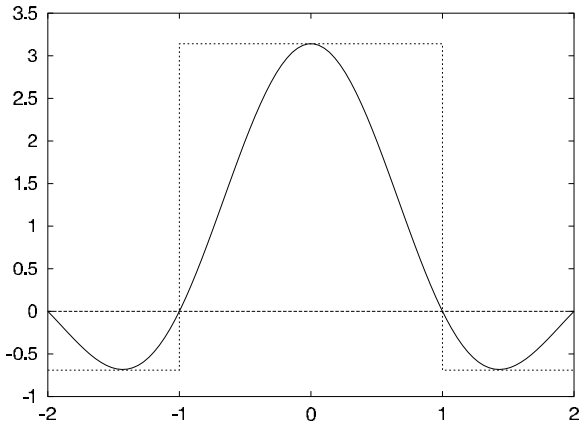

Figure 2. The theoretical continuous curve can only be approximated over a discretized grid (dashed steps) up to a resolution which allows separating positive and negative parts; the zero-crossings then correspond to pixel boundaries. For that reason, the number of zero-crossings determines the minimum attainable resolution.

applying an appropriate wavelet Ψ capable of canceling polynomials up to an order n greater than the maximum expected h in the multifractal. For a multiaffine signal $s(\mathbf{x})$, equation (22), it follows [19, 8] that any admissible wavelet Ψ verifies[5]

$$T_\Psi s(\mathbf{x}, r) = \alpha_\Psi(\mathbf{x})\, r^{\gamma(\mathbf{x})} + O(r^{\gamma(\mathbf{x})}). \tag{23}$$

On the other hand, when the long-range correlation term $L(\mathbf{x})$ can be expanded in a Taylor expansion around the point $\mathbf{x}$, then for any wavelet Ψ which vanishes any polynomial in the components $x_1, \ldots, x_d$ of the position vector $\mathbf{x}$ up to the order $n-1$, it follows that

$$T_\Psi L(\mathbf{x}, r) = l_\Psi(\mathbf{x})\, r^n + o(r^n). \tag{24}$$

Hence, when the measured signal $s_{\mathcal{M}}(\mathbf{x})$ consists of the sum of a multiaffine part and of a long-range correlation term $s_{\mathcal{M}}(\mathbf{x}) = s(\mathbf{x}) + L(\mathbf{x})$, we can recover the correct singularity exponents $\gamma(\mathbf{x})$ up to the order n, for a wavelet vanishing polynomials up to the order $n-1$, because

$$T_\Psi s_{\mathcal{M}}(\mathbf{x}, r) = \alpha_\Psi(\mathbf{x})\, r^{\gamma(\mathbf{x})} + o(r^{\gamma(\mathbf{x})}) \tag{25}$$

for all $\gamma(\mathbf{x}) < n$. A usual choice for n is $n = 2$, probably due to the fact that the typical value for H_C is 1. Note, however, that there are reasons to limit the maximum filtered polynomial order. A wavelet capable of filtering higher and higher order polynomials can be generated by successive differentiation of a basis wavelet. However, as the differentiation order increases, the number of zero-crossings in the wavelet also grows up, what limits the minimum resolution that the wavelet can attain; see figure 2. As a consequence, the spatial localization of the singularities is worse as the order n of filtered polynomials is increased. Because of this effect, a compromise must be reached.

Contamination of a multiaffine signal by smooth long-range correlations is not the only problem that may appear. Some more complicated situations may happen, and the one which has been studied in greatest depth is the apparition of oscillating singularities [60, 61]. For

[5] Note that in the most frequent formulations multiaffine functions are analyzed with directional wavelets or even with wavelet distributions which have only support over a given direction. However, there is no reason to impose this restriction in general.

those cases, it was proposed to extract the scale-space skeleton of maxima lines for the wavelet transform, that is, those lines in the $(\mathbf{x}, r)$ space for which $|T_\Psi s(\mathbf{x}, r)|$ were local maxima for fixed r. It was conjectured by Mallat [62] that the maxima lines could contain enough information to fully reconstruct the whole signal. Methods such as WTMM [8, 26, 29] take advantage of these ideas. Note however, that these techniques are applied in the canonical framework but cannot be implemented according to the microcanonical formalism because, by definition, the singularity exponents are computed at the maxima lines only, which are required to be isolated points at each fixed value of r [26] (although some attempts to extend WTMM to obtain an estimate of $h(\mathbf{x})$ at any point $\mathbf{x}$ have been done [58]). In addition, WTMM requirement of having isolated singularities poses many problems when the signal under analysis is formed by singularity components which are dense sets [53].

4.2.2. Multifractal measures. Another important concept in the multifractal microcanonical formalism concerns the definition and construction of multifractal measures. They are designed to reveal the existence of power-law correlations in signals s which are not simply directional (as with multiaffine functions) but which extend over a whole region and to characterize the regularity of the function at a given point. However, instead of taking variable-scale increments centered on the studied point (which are more affected by error in real, experimental situations), one integrates all the variations of the function around that point at different scales. This integration allows us to remove some fluctuations and to obtain a better idea on the behavior of the function when real data are processed. For a given signal s which has an underlying multifractal structure, a reasonable guess for a multifractal measure $\mu_\mathcal{D}$ is the following:

$$\mathrm{d}\mu_\mathcal{D} = \mathcal{D}s \, \mathrm{d}\mathbf{x} \tag{26}$$

(i.e. a measure having density $\mathcal{D}s$ w.r.t. to the Lebesgue measure $\mathrm{d}\mathbf{x}$) where $\mathcal{D}$ is an appropriate differential operator, to be determined. We will discuss on the properties of $\mathcal{D}$ a bit later; so far, let us say that obviously the operator should be such that $\mathcal{D}s$ is a locally integrable function. By construction, $\mu_\mathcal{D}$ is absolutely continuous with respect to the Lebesgue measure.

A measure $\mu_\mathcal{D}$ as the one defined above is a multifractal measure if for any point $\mathbf{x} \in \Omega$ one has:

$$\mu_\mathcal{D}(B_r(\mathbf{x})) = \alpha_\mathcal{D}(\mathbf{x}) r^{h(\mathbf{x})+d} + o(r^{h(\mathbf{x})+d}) \tag{27}$$

where $B_r(\mathbf{x})$ stands for the ball of radius r centered at $\mathbf{x}$. The shift d (space dimension) is introduced to remove the contribution due to the integral, hence capturing the behavior specific to the function $\mathcal{D}s$.

There is no known way to define the operator $\mathcal{D}$ in order to generate a multifractal measure for a signal which is known to have intrinsic multifractal structure. However, some general principles are very helpful to find an appropriate form for it. For instance, many signals are known to possess strong spatial correlations, manifested as a f^{-2} scaling in the power spectrum. If $\mathcal{D}$ is the identity operator, the integral in equation (27) would be dominated by the mean value of s on the ball $B_r(\mathbf{x})$, which is far from zero due to the lack of stationarity. As discussed in section 2, the derivative renders the function stationary, and hence the measure of a ball will reflect the actual singular structure around the point. This idea suggests to define a vector-valued measure with the choice $\mathcal{D} = \nabla$, which has the advantage of leading to a linear increment as those used in the definition of multiaffine functions when $d = 1$ (as gradients are approximated on real data by finite increments). However, other reasons such that numerical stability make preferable to define the operator as $\mathcal{D}s = \|\nabla s\|$. It has been successfully used

in [21, 22, 25, 36, 51, 52] and will be our choice in this paper; the associated measure μ is given by

$$\mu(A) = \mu_{\|\nabla\|}(A) = \int_A \|\nabla s\|(\mathbf{x})\,\mathrm{d}\mathbf{x} \tag{28}$$

for any measurable set A. Note that for locally integrable ∇s the measure μ is the absolute variation of μ_∇, that is, $\|\mu_\nabla\| = \mu$. It follows that the scaling exponents obtained for μ_∇ are the same as those of μ.

It is interesting to note that this property allows us to relate multiaffine functions to multifractal measures. Let us assume that s is multiaffine, in the sense that for any admissible wavelet Ψ equation (23) holds. For a particular wavelet Ψ which is the gradient of another function, $\Psi = \nabla\Phi$, we obtain

$$\begin{aligned} T_\Psi s(\mathbf{x}, r) &= s * \Psi_r(\mathbf{x}) = s * (\nabla\Phi)_r(\mathbf{x}) = s * (r\nabla\Phi_r)(\mathbf{x}) \\ &= r\nabla s * \Phi_r = rT_\Phi \nabla s(\mathbf{x}, r). \end{aligned} \tag{29}$$

Applying equation (23) to the expression above it follows that

$$T_\Phi \nabla s(\mathbf{x}, r) = \alpha_\nabla(\mathbf{x})\, r^{h(\mathbf{x})} + o(r^{h(\mathbf{x})}) \tag{30}$$

where $h(\mathbf{x}) = \gamma(\mathbf{x}) - 1$. It suffices now to define Φ as the set function associated with the unit radius, $\Phi = 1_{B_1(\mathbf{0})}$ to find

$$\mu_\nabla(B_r(\mathbf{x})) = r^d\, T_\Phi \nabla s(\mathbf{x}, r) = \alpha_\nabla(\mathbf{x})\, r^{h(\mathbf{x})+d} + o(r^{h(\mathbf{x})+d}). \tag{31}$$

We conclude that if s is a multiaffine function, then the associated measure μ is a multifractal measure. In addition, the singularity exponent of the measure at any point $\mathbf{x}$, $h(\mathbf{x})$, is simply related to the multiaffine exponent $\gamma(\mathbf{x})$ at the same point: they differ by a -1 shift, a property that had been reported before [51, 63].

As for multiaffine functions, multifractal measures can be wavelet transformed in order to filter additive long-range correlations which could affect the evaluation of high-order singularities. However, taking into account the differential character of the measure density this type of filtering is generally unnecessary. Let us concentrate in our choice $\mathcal{D} = \|\nabla\|$, and, as before, let us suppose that the measured signal $s_\mathcal{M}$ can be represented as the sum of a multiaffine part s and the long-range correlation term L. As we have just shown, the multiaffine part will lead to a multifractal measure in which the exponents will be shifted by -1 with respect to those of the multiaffine function. On the other hand, the regular part will define a measure with density ∇L, which will also be differentiable and only affects the exponents $h(\mathbf{x}) > 1$. Hence, the range of singularities which are not affected by the presence of the long-range correlation has been expanded by 1. In many practical situations this is sufficient, as the singularities which could be affected are of so high order that they are anyway almost impossible to evaluate. But there is a different reason supporting the use of wavelet transforms of a multifractal measure (rather, with the wavelet transform of the density $\mathcal{D}s$): the necessity of providing good interpolation schemes for discretized signals in order to evaluate the singularity exponents.

A final comment concerning wavelets. The wavelet Ψ must verify some requirements, as the behavior of its tail at infinity may alter the values of the singularity exponents. When the position variable $\mathbf{x}$ goes to infinity, the wavelet must decay faster than $\|\mathbf{x}\|^{-h_m-d}$ where h_m is the maximum value that the singularities $h(\mathbf{x})$ can take. The proof is given in the appendix. This requirement can also be formulated in the opposite way: if the wavelet behaves like $\Psi(\mathbf{x}) \sim \|\mathbf{x}\|^{-n_0}$ when $\|\mathbf{x}\| \to \infty$; hence,

$$T_\Psi \|\nabla s\|(\mathbf{x}, r) = \alpha_\Psi(\mathbf{x})\, r^{h_\Psi(\mathbf{x})} + o(r^{h_\Psi(\mathbf{x})}) \tag{32}$$

where

$$h_\Psi(\mathbf{x}) = \begin{cases} h(\mathbf{x}), & h(\mathbf{x}) < n_0 - d \\ n_0 - d, & h(\mathbf{x}) \geqslant n_0 - d. \end{cases} \tag{33}$$

These results make reasonable to use a wavelet that decreases faster than any power law. However, there is a trade-off between decrease speed and spatial localization of singularities: wavelets with very steep decrease should be defined over minimum scales extending several discretization units in order to provide a good enough interpolation but, consequently, the uncertainty in the spatial localization is greater as this is function of a minimum scale. In the next subsection, we will illustrate this issue with some examples.

4.3. Decomposing the signal: multifractal components

Since the microcanonical multifractal formalism allows us to determine the singularity exponents of a signal at any point it is an excellent method to analyze some dynamical properties of the physical system under study though the quality on the dynamical analysis will be conditioned by the accuracy in the assessment of the different multifractal components and the corresponding singularity exponents. One has to determine the value of $h(\mathbf{x})$ with the smallest possible error and also to minimize the spatial uncertainty about the actual position of the evaluated exponent. In this scenario, it is crucial to pay attention to a very special component, the so-called most singular component[6] (MSC). The MSC plays a central role in the description of multifractal physical systems. Geometrically speaking, it is the singularity component associated with the smallest possible value h_∞, finite for physical signals. We will denote this set by $\mathcal{F}_\infty$; $\mathcal{F}_\infty = \mathcal{F}_{h_\infty}$. In experimental situations [51, 64], the MSC must be defined as a central value with a given quantization Δh, namely

$$\mathcal{F}_\infty = \{\mathbf{x} \mid h(\mathbf{x}) \in]h_\infty - \Delta h, h_\infty + \Delta h[\}. \tag{34}$$

The MSC comprises the points where sharp, sudden local variations take place. For illustrations purposes, let us mention that it is characterized by the presence of edges and contours in the case of natural images [51, 64], periods with high volatility changes in the case of econometric times series [25] or transitions in the case of physical signals [21, 52]. It is the component with the highest amount of information and among different outstanding properties it allows us to reconstruct the whole signal. Details will be given in the next section. The aforementioned reasons justify the search and development of techniques designed to determine accurately the MSC. In this context, wavelet analysis is an excellent tool to carry out the task. However, the design of appropriate wavelets, probably depending on specific contexts of application, is still an open question. The design always implies a trade-off: as the range of singularities it is able to resolve increases the quality of the spatial localization of these singularities decreases.

4.4. Experimental application of the microcanonical framework

In this section, we want to illustrate the ideas presented so far. As benchmarks we will study our example signals checking if the microcanonical multifractal formalism can be applied with a reasonable accuracy, emphasizing all the steps required to perform the analysis.

4.4.1. Test on multiaffinity. The first check is to determine if the test signals can be considered multiaffine functions in the most general formulation. This means that

[6] Also called most singular manifold in the literature, although it need not to be a topological manifold.

- equation (25) is satisfied taking into account the numerical limitations. This requires that a large enough amount of points exhibit good correspondence with equation (25) for a sufficiently large range of scales;
- the singularity spectra derived at each scale should fit, within the allowed numerical accuracy, the same convex curve.

Concerning the first point, we propose a simple test on the validity of equation (25). It consists in evaluating, for each point, the wavelet projections of the signal at different scales. Then a log–log linear regression is performed in order to compute $\gamma(\mathbf{x})$. We will consider that equation (25) is satisfied if the regression coefficient of this fit is large enough for all but a negligible amount of points. We have used as wavelets nth-order Gaussians and nth-order β-Lorentzians for orders $n \in \{1, 2\}$ and exponents $\beta \in \{0.5, 1, 1.5, 2\}$. The signals were projected on various ranges of scales. The minimum value r_1 is limited from below by the wavelet resolution scale, r_Ψ, which depends on the wavelet Ψ we intend to use (see discussion in section 4.2.1). The maximum scale r_2 is only limited by the size of the signal. We will denote the ratio of scales κ, $\kappa = r_2/r_1$, as the 'scale width'. Obviously, we can define a range of scales by giving the minimum scale and the scale width. For our test, we have tried different minimum scales (from 1 to 10 wavelet resolution scales) and several scale widths (from 2 to 50). A typical choice is $r_1 = r_\Psi$ and $\kappa = 10$, which is a compromise between taking a wide enough range of scales and still have good spatial localization of the singularity values.

The results show that multiaffinity is a bad hypothesis for our test signals. For instance, for the typical scale range ($r_1 = r_\Psi, \kappa = 10$), less than 50% of the points had regressions coefficient above 0.8 for the MeteoSat image. In the case of the Telefónica^{TM} series the situation is even worse, having less than 25% of points with regression above 0.8. Similar results were obtained for the other ranges. Hence, we consider that these two signals are not multiaffine functions. We propose two reasons that could justify why the signals deviate significantly from multiaffinity: on one hand, the directional dependence of the Hölder exponent, that we neglected as a hypothesis; on the other hand, the numerical instabilities associated with the use of very structured wavelets with several zero crosssings.

4.4.2. Test on multifractal measures. A completely different situation is presented when the test signals are analyzed as multifractal measures. As before, the analysis proceeds in two steps. First, we have to verify if equation (32) holds for all the points over several ranges in scale, when an appropriate wavelet is employed. To perform the analysis we have first used the Gaussian wavelet, as this wavelet does not impose any restriction on the observable range of singularities (see the appendix). For the MeteoSat image, we obtain that more than 99% of the points had regression coefficient above 0.9 for any of the tested ranges (that is, $r_1 \in [r_\Psi, 10r_\Psi]$ and $\kappa \in [2, 50]$). In the case of the Telefónica^{TM} series, we obtain similar results: 95% points had regression coefficient above 0.9 for all the scale ranges. In figure 3 we present the empirical distribution of values of h for both signals for $r_1 = r_\Psi$ and $\kappa = 10$.

The second part of the test consists in determining the singularity spectrum at different scales and then verify that we get the same convex curve. To evaluate $D(h)$, we have applied equation (21), where the resolution scale r_0 is estimated from the data resolution: $r_0 = 1/q$ for series consisting of q equally spaced points while $r_0 = 1/\sqrt{n_x n_y}$ for images having $n_x \times n_y$ pixels. We changed the resolution of the data (or, equivalently, of the minimum scale in the wavelet) in powers of 2. The results are summarized in figure 4. The correspondence is very good, so we state that the second condition is also verified. We conclude that both signals define multifractal measures and that we can apply in this way the microcanonical framework.

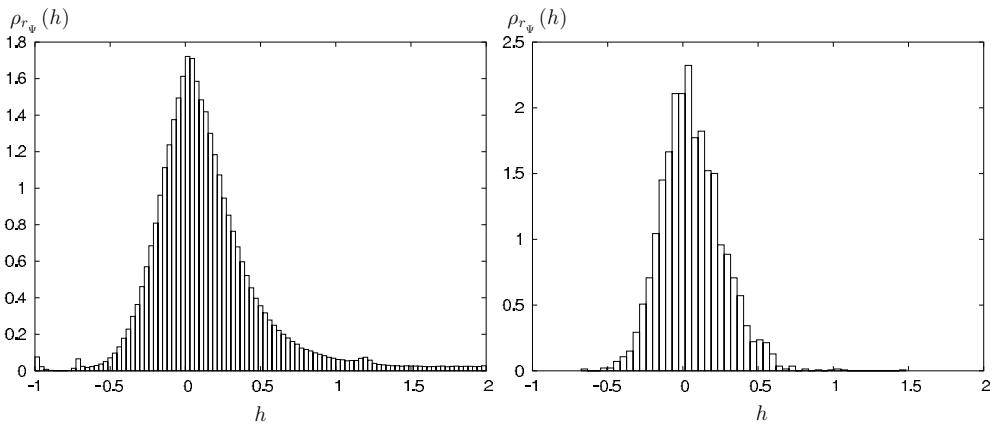

Figure 3. Empirical singularity distributions at resolution scale for Meteosat (left) and Telefónica (right).

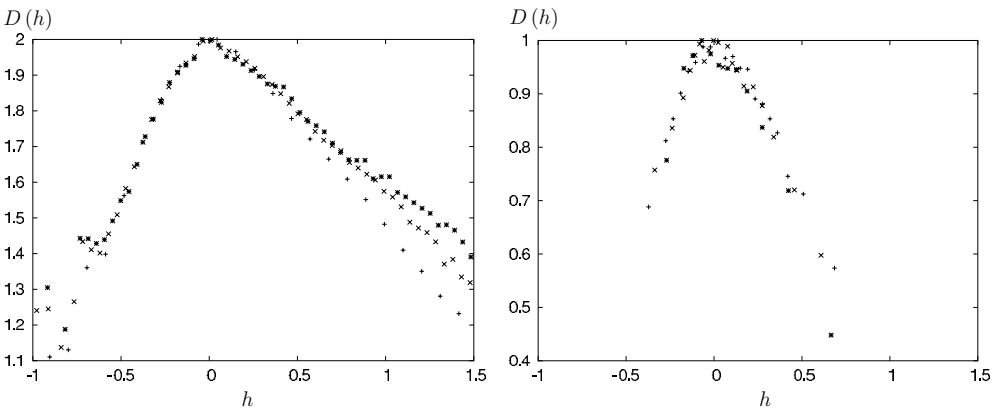

Figure 4. Test on the multiscale and convex character of the singularity spectra estimated for MeteoSat (left) and Telefónica (right). The curves correspond to original resolution (+), 2 times reduced ($\times$) and 4 times ($*$) reduced.

4.4.3. Signal decomposition. Once the signals have been proved to possess multifractal structure, it is interesting to explicitly perform the multifractal decomposition, in order to study the different fractal components and relate them to the dynamical properties of the system. In figure 5, we show a representation of the singularity exponents obtained with the Gaussian wavelet.

We have also verified that Lorentzian wavelets give similar results, with good regression exponents for the majority of points. Confirming the derivation given in the appendix and according to equation (33), the estimated values of singularity exponents are truncated beyond a value which depends on the tail of the wavelet. Hence, as β-Lorentzians decay as $\|\mathbf{x}\|^{-2\beta}$ we find that the truncation exponents are $h_\beta = 2\beta - d$. Up to h_β the distribution of exponents is in good correspondence with that obtained for the Gaussian wavelet for the equivalent scale range, and hence we obtained the same estimates for the singularity spectrum over the resolved range of singularities. In figures 6 and 7, we summarize the results for the MeteoSat image, and similar results are obtained for Telefónica series. In the rest of this section, we

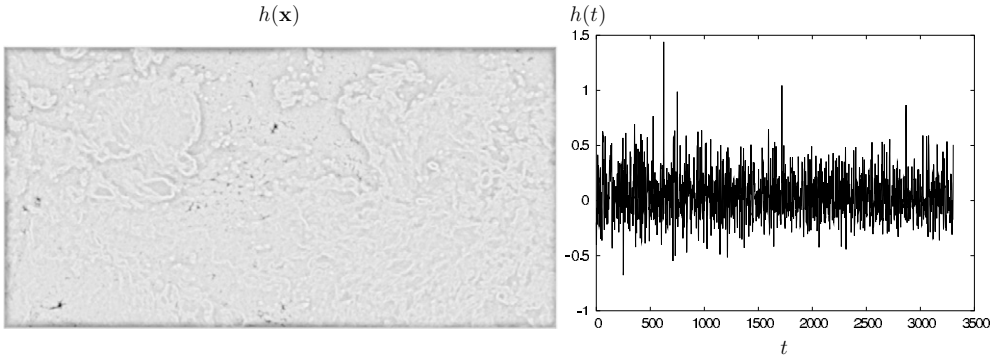

Figure 5. Left: Gray-level representation of the singularity exponents for a MeteoSat image acquired in the thermal infrared range; the brightest is the point, the most singular (i.e., smallest) is the value represented. Right: Series of singularity exponents for Telefónica series. For both graphs the Gaussian wavelet was used.

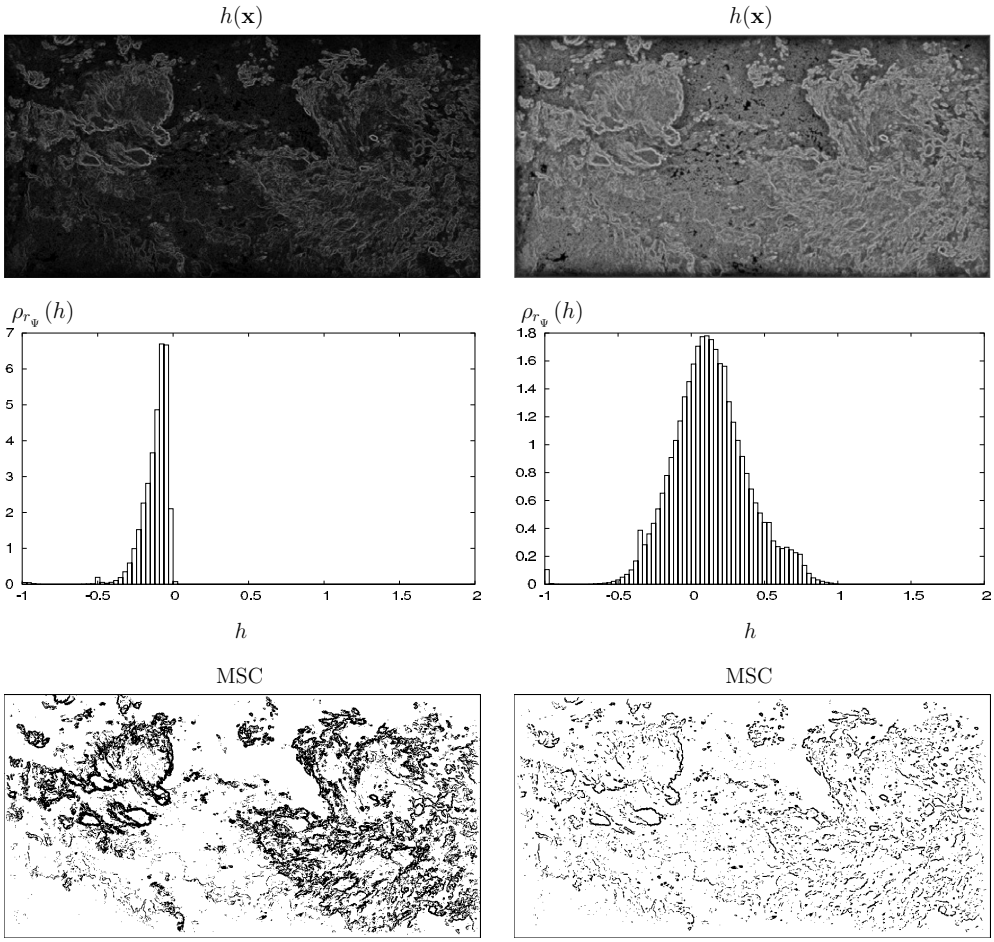

Figure 6. From top to bottom: Gray-level representation of the singularity exponents, empirical distribution of singularity exponents and estimated most singular component ($h < -0.2$). Left: Results for L_1. Right: Results for $L_{1.5}$.

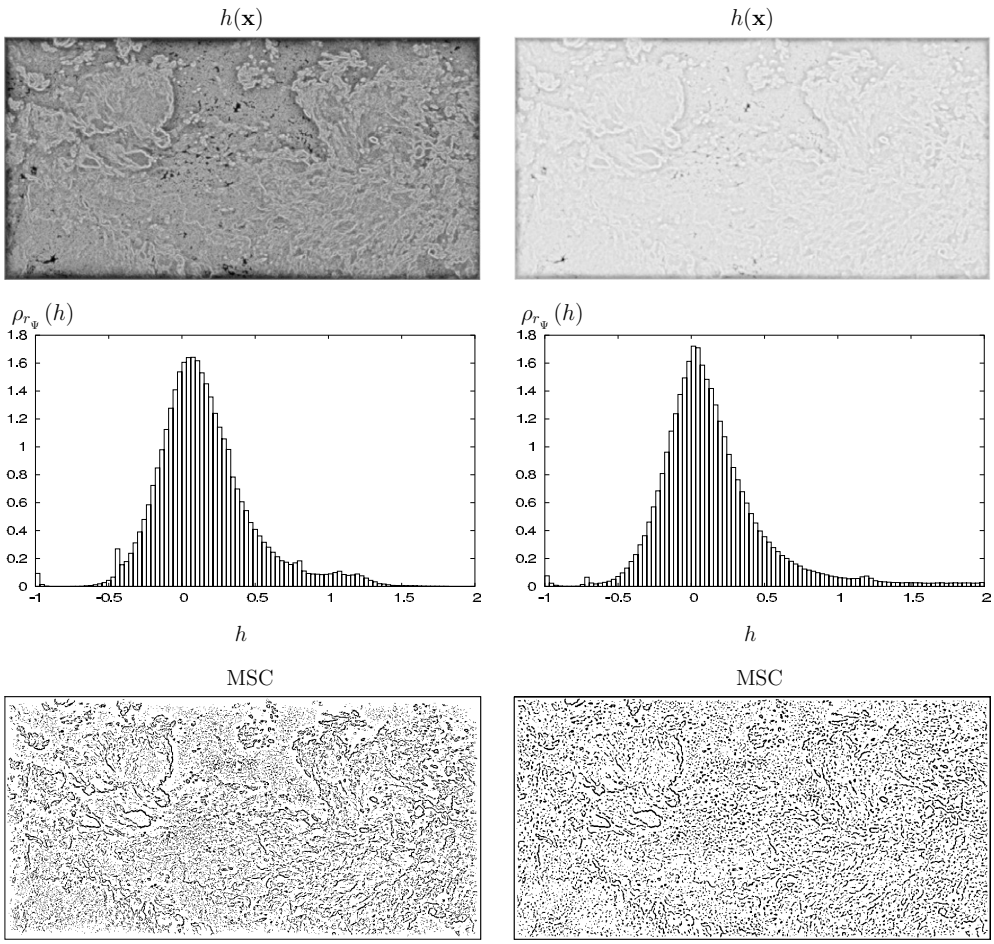

Figure 7. From top to bottom: Gray-level representation of the singularity exponents, empirical distribution of singularity exponents and estimated most singular component ($h < -0.2$). Left: Results for L_2. Right: Results for G.

will concentrate on the MeteoSat image because it is easier to illustrate geometrical concepts using signals defined over a spatial domain.

Concerning multifractal components, we have already discussed how important is to determine the MSC with high accuracy. In this study, the estimates for the MSC are calculated using the range with the finest spatial accuracy ($r_1 = r_\Psi, \kappa = 2$). The MSC is actually evaluated as the set of points below a given threshold h_θ, namely

$$\mathcal{F}_\infty = \{\mathbf{x} \mid h(\mathbf{x}) < h_\theta\} \tag{35}$$

that for the distributions presented here corresponds almost exactly[7] with the application of equation (34) for $h_\infty = -0.4$ and $\Delta h = 0.2$, which is in fact a reasonable quantization. Looking at the figures 6 and 7 we observe that wavelets G and L_2 are able to evaluate higher order singularities but losing spatial discrimination, as was argued in section 4.2.2. On the other hand, L_1 provides fine spatial determination of the MSC, but at the cost of being unable to

[7] The only points not included are those close to $h = -1$, which in fact are boundary points: the limits of the image induce step-like transitions which are associated with a $h = -1$ exponent [19, 51].

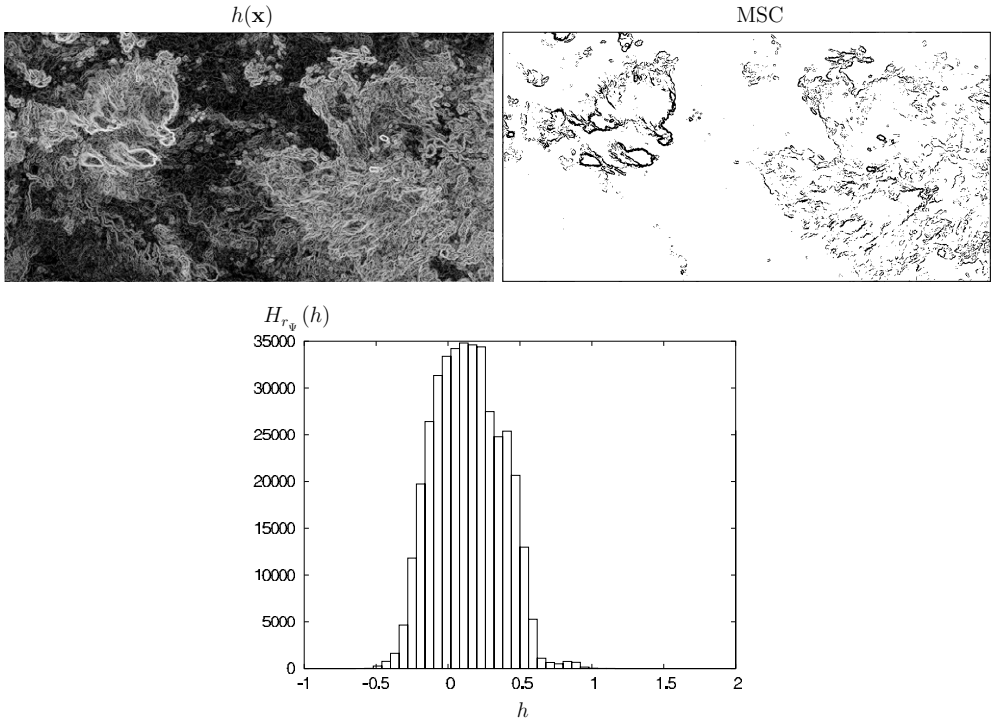

Figure 8. Top: Gray-level representation of the evaluated singularity exponents for MeteoSat image, using the optimized L_1 wavelet (left) and associated MSC ($h < -0.2$) (right). Bottom: Empirical histogram of singularities.

differentiate singularities above $h = 0$. In fact, constructing an appropriate wavelet optimizing both the resolved singularity range and the spatial resolution is highly non-trivial. After years of study, we have developed a reasonably efficient wavelet. It is an optimized version of L_1, designed to produce as good reconstruction as possible (see the next section), and is defined by its numerical weights on a discrete array. In figure 8, we show the results of its application to the MeteoSat image. Anyway, wavelet design is an open question which would deserve dedicated studies.

5. Reconstructing the signal

In this section, we go one step beyond and show a remarkable feature intimately related to the microcanonical character of the analysis performed so far: the signal can be reconstructed. The implications of this fact are enormous as we will describe throughout the paper.

5.1. The multiplicative cascade in the microcanonical formulation

According to the theoretical arguments that were discussed in section 4.2.1, the singularity exponents of a physical multiaffine signal must be bounded from below: $\gamma(\mathbf{x}) > 0$ or, equivalently, $h(\mathbf{x}) > -1$ (due to the relation $h = \gamma - 1$ that was discussed in section 4.2.2). In the case of more general physical signals, if we suppose that the associated multifractal measure is bounded on compacts subsets, which is quite reasonable, then the associated singularities are also bounded. The experiments on real data confirm this theoretical bound:

for the diverse ranges of scales tried, the exponents h for the multifractal measures derived from different signals (in particular for the two examples we have presented here) are bounded by -1 (look at the empirical singularity distributions in figures 6 and 7). Then, there exists a lower bound h_∞ and its associated component, the MSC $\mathcal{F}_\infty$. The presence of the MSC can be recognized in the shape of the canonical exponents τ_p, as the largest order moments are dominated by the MSC, $\tau_p = h_\infty p + o(p)$ for $p \gg 1$. According to Parisi and Frisch's formula, equation (18), we can relate each value of p to a value of h, in the way $h(p) = \frac{\mathrm{d}\tau_p}{\mathrm{d}p}$ and analogously for each value of h a value of p, $p(h) = \frac{\mathrm{d}D(h)}{\mathrm{d}h}$. So, the correspondence between values of the singularity exponents h and orders of moment p is one to one. This makes tempting to establish a link between the cascade process discussed in section 3.2, which distributes energy from larger to smaller scales, and the hierarchy of singularity components $\mathcal{F}_h$. The goal would be to describe the cascade as an injection process among the different singularity components. As a prerequisite, we need to re-interpret the cascade: it represents an energy transfer between scales, and it should be written in terms of energy transfer between different order p-moments at fixed scale. She and Leveque [65] derived a relation of this kind for the case of log-Poisson multifractals. In the following, we will present a more general version of their derivation. For the sake of simplicity, we will assume that in equation (10) the derivative with respect to p of α_p is negligible in comparison with the derivative of r^{τ_p}; this is a reasonable approximation when $r \ll 1$. Hence, for a fixed quantum Δp let us define the p-dissipation term, $\epsilon_r^{(p,\Delta p)}$ as

$$\epsilon_r^{(p,\Delta p)} = \left[\frac{\langle|\mathbb{T}_r\mathbf{s}|^{p+\Delta p}\rangle}{\langle|\mathbb{T}_r\mathbf{s}|^{p}\rangle}\right]^{\frac{1}{\Delta p}}. \tag{36}$$

The p-dissipation term can be interpreted as the part of $\mathbb{T}_r s$ which can be retrieved from the range of moments going from p to $p + \Delta p$. From the physical point of view, we can say that this variable is the sum of the contributions to $\mathbb{T}_r s$ by the singularity components with singularity exponents in the range $]h(p + \Delta p), h(p)[$. We can see that this variable take only contributions from this subset of components: according to equation (10) we obtain

$$\epsilon_r^{(p,\Delta p)} = r^{\frac{\tau_{p+\Delta p}-\tau_p}{\Delta p}} + o\left(r^{\frac{\tau_{p+\Delta p}-\tau_p}{\Delta p}}\right) = r^{\bar{h}_{\Delta p}(p)} + o(r^{\bar{h}_{\Delta p}(p)}) \tag{37}$$

where we have introduced the average singularity exponent of order p, $\bar{h}_{\Delta p}(p)$,

$$\bar{h}_{\Delta p}(p) = \frac{\tau_{p+\Delta p} - \tau_p}{\Delta p} = \frac{1}{\Delta p}\int_p^{p+\Delta p} \mathrm{d}q\, \frac{\mathrm{d}\tau_p}{\mathrm{d}p}(q) = \frac{1}{\Delta p}\int_p^{p+\Delta p} \mathrm{d}q\, h(q). \tag{38}$$

Let us now suppose that the system is a log-Poisson multifractal. log-Poisson multifractals have been used quite often to model experimental canonical exponents obtained in FDT experiences [47, 66–68]. Something interesting about log-Poisson multifractals is that the canonical exponents τ_p can be parameterized using the two variables defining the MSC: the singularity h_∞ and the dimension of the associated component, $D_\infty = \dim(\mathcal{F}_\infty)$. The exponents τ_p are given by the following expression:

$$\tau_p = h_\infty p + (d - D_\infty)(1 - \beta^p) \tag{39}$$

where the parameter β represents the effective injection rate among scales, $0 < \beta < 1$, and can be related to the other two free parameters due to translational invariance [51, 66],

$$\beta = 1 + \frac{h_\infty}{d - D_\infty} \tag{40}$$

from where it follows $h_\infty < 0$ and $-h_\infty < d - D_\infty$ as extra constraints on the parameters. Applying equation (39) to the definition of the p-dissipation term, equation (37), we obtain

$$\bar{h}_{\Delta p}(p) = h_\infty + (d - D_\infty)\beta^p \frac{1-\beta^{\Delta p}}{\Delta p} = h_\infty \left(1 - \frac{\beta^p}{1-\beta}\frac{1-\beta^{\Delta p}}{\Delta p}\right). \tag{41}$$

where we have used equation (40). It follows trivially from equation (41) that $\lim_{p\to\infty} \bar{h}_{\Delta p}(p) = h_\infty$, and in fact the different values of $\bar{h}_{\Delta p}(p)$ represent the averages over bunches of singularity components, ordered from the MSC ($p = \infty$) to the least singular one ($p = -\infty$). If we now apply equation (41) to evaluate $\bar{h}_{\Delta p}(p + \Delta p)$ we obtain

$$\bar{h}_{\Delta p}(p + \Delta p) = h_\infty \left(1 - \frac{\beta^{\Delta p}}{1-\beta}\frac{1-\beta^{\Delta p}}{\Delta p}\right) + \beta^{\Delta p}\bar{h}_{\Delta p}(p). \tag{42}$$

In the original derivation from She and Leveque's work, $\Delta p = 1$ and the relation above simplifies to $\bar{h}_1(p+1) = h_\infty(1-\beta) + \beta\bar{h}_1(p)$. Therefore

$$\epsilon_r^{(p+1,1)} = \left(\epsilon_r^{(\infty,1)}\right)^{1-\beta}\left(\epsilon_r^{(p,1)}\right)^{\beta} \tag{43}$$

and in general, for any $q > 0$

$$\epsilon_r^{(p+q,1)} = \left(\epsilon_r^{(\infty,1)}\right)^{(1-\beta)(\beta^0+\cdots+\beta^{q-1})}\left(\epsilon_r^{(p,1)}\right)^{\beta^q} \tag{44}$$

and in particular, when $p = 0$ we obtain that

$$\epsilon_r^{(q,1)} = \left(\epsilon_r^{(\infty,1)}\right)^{(1-\beta)(\beta^0+\cdots+\beta^{q-1})}\left(\epsilon_r^{(0,1)}\right)^{\beta^q}. \tag{45}$$

Taking into account that $(1-\beta)\sum_{i=0}^{q-1}\beta^i = 1 - \beta^q$ and that $\epsilon_r^{(0,1)} = 1$ in the log-Poisson model, it follows

$$\epsilon_r^{(q,1)} = \left(\epsilon_r^{(\infty,1)}\right)^{1-\beta^q}. \tag{46}$$

This can be interpreted as an energy transfer from the MSC, represented by $\epsilon_r^{\infty,1}$, to any moment q by successive steps of energy transfer. The continuous limit of this expression is obtained by letting $\Delta p \to 0$. Recalling that $\lim_{\Delta p\to 0}\bar{h}_{\Delta p}(p) = h(p)$, taking limits of vanishing Δp in both sides of equation (41) we get

$$h(p) = h_\infty\left(1 + \log\beta\frac{\beta^p}{1-\beta}\right) \tag{47}$$

and now, defining $\epsilon_r^{(p)} = \lim_{\Delta p\to 0}\epsilon_r^{(p,\Delta p)}$ we conclude

$$\epsilon_r^{(p)} = \left(\epsilon_r^{(\infty)}\right)^{1+\log\beta\frac{\beta^p}{1-\beta}}. \tag{48}$$

In fact, equation (48) is the particular expression for log-Poisson multifractals of a more general relation, namely

$$\epsilon_r^{(p)} = \left(\epsilon_r^{(\infty)}\right)^{h(p)/h(\infty)}. \tag{49}$$

She and Leveque's intuition was in fact that the cascade could be interpreted in a microcanonical way: if it is possible to construct variables $e_r^{(p)}(\mathbf{x})$ such that $\langle e_r^{(p)}\rangle = A_p^e\epsilon_r^{(p)}$ and for which equation (49) is valid, and not only for the first-order moments, namely

$$e_r^{(p)}(\mathbf{x}) \doteq \alpha_p^e(\mathbf{x})\left(e_r^{(\infty)}(\mathbf{x})\right)^{h(p)/h(\infty)} \tag{50}$$

where now the equality holds in distribution only. In the microcanonical formalism equation (50) trivially holds: the variables $e_r^{(p)}(\mathbf{x})$ are the restriction of $\mathbb{T}_r s(\mathbf{x})$ to the singularity component $\mathcal{F}_{h(p)}$. Then, according to equation (32), $\mathbb{T}_r s(\mathbf{x})_{|\mathcal{F}_{h(p)}} = \alpha_\Psi(\mathbf{x})\, r^{h(p)}$ and equation (50) follows. According to the discussions in this section, we consider equation (50) as the expression of the energy cascade in the microcanonical framework.

5.2. *Reconstructing a signal from its most singular component*

Although appealing, equation (50) does not imply that the energy, starting from the MSC, is transmitted point by point from one component to the others; rather, it simply implies that the distributions of the variables behave as that. What is interesting in equation (50) is that the relation between any component and the MSC is deterministic, and it is completely defined by the ratio $h(p)/h(\infty)$. For that reason, Turiel and del Pozo [69] proposed a deterministic algorithm to reconstruct the signal from the MSC, according to some general requirements, compatible with the observed statistical symmetries. In the following, we detail the reconstruction algorithm and then we will discuss it in the perspective of the cascade and regarding its experimental performance.

We will work with the standard multifractal measure $\mu = \mu_{\|\nabla s\|}$. The goal is to obtain a functional $\mathcal{G}$ such that it could regenerate the values of the measure from its restriction to the MSC $\mathcal{F}_\infty$. Expressed in terms of the measure density, which is $\|\nabla s\|$, we intend to reproduce $\|\nabla s\|$ from $\|\nabla s\|_{|\mathcal{F}_\infty}$. The five conditions imposed on the mapping $\mathcal{G}$ in [69] are the following:

- it is deterministic,
- linear,
- translationally invariant,
- isotropic,
- and it leads to the known power spectrum.

Under this set of assumptions there exists only one possible kernel $\mathcal{G}$, as we will next show. The requirements can be applied one by one, to define the kernel.

5.2.1. Determinism. This property is justified by the characteristics of the microcanonical cascade discussed in the previous section. If the reconstruction is deterministic, we can consider the functional $\mathcal{G}$ not as a random variable, but as an actual function $\mathcal{G} : \mathcal{L}^1_{\mathbb{C}}(\mathbb{R}^d) \longrightarrow \mathcal{L}^1_{\mathbb{C}}(\mathbb{R}^d)$. The following expression holds

$$\|\nabla s\|(\mathbf{x}) = \mathcal{G}(\|\nabla s\|_{|\mathcal{F}_\infty})(\mathbf{x}) \tag{51}$$

that is, the value of $\|\nabla s\|$ at any point is a function $\mathcal{G}$ of the values of $\|\nabla s\|$ over the MSC. Stated differently, $\mathcal{G}$ permits the *reconstruction* of a signal on its whole domain space giving only information of that signal on the subset $\mathcal{F}_\infty$.

5.2.2. Linearity. This requirement cannot be justified *a priori* by any known property of the ensemble of multifractals, and is introduced only for mathematical convenience. Under the linearity assumption, it does not make sense to work with the modulus of the gradient, as the modulus of the gradient is not a linear operator. Instead, we generalize equation (51), changing $\|\nabla s\|$ by ∇s, as the gradient operator is linear. Anyway, the gradient itself contains more information than its modulus, so if the reconstruction is possible from the modulus, it should also be possible from the gradient. We assume in addition that $\mathcal{G}$ is a continuous linear operator, so we look for an integral representation of $\mathcal{G}$, in the way

$$\nabla s(\mathbf{x}) = \mathcal{G}(\nabla s_{|\mathcal{F}_\infty})(\mathbf{x}) = \int_{\mathcal{F}_\infty} \mathrm{d}l(\mathbf{y})\, \mathbf{G}(\mathbf{x}, \mathbf{y}) \nabla s(\mathbf{y}) \tag{52}$$

where $\int_{\mathcal{F}_\infty} \mathrm{d}l(\mathbf{y})$ means integration over the MSC. It is a hard task to precise under which conditions the MSC is a Borelian subset of Euclidean space since it completely depends on the geometry and particularities of the system under analysis. For the moment, we assume the MSC to be measurable and $\int_{\mathcal{F}_\infty} \mathrm{d}l(\mathbf{y})$ is the integral representation of the canonically associated Lebesgue measure, probably by means of the Hausdorff measure [5] (assuming that the MSC

is a regular fractal). Looking at equation (52) we observe that we now represent the linear operator $\mathcal{G}$ by means of its $d \times d$ matrix density, denoted by $\mathbf{G}(\mathbf{x}, \mathbf{y})$. We will represent the matrix element as $G_{ij}(\mathbf{x}, \mathbf{y})$ where $i, j = 1, \ldots, d$. If we denote by $\partial_j s$, $j = 1, \ldots, d$ the components of ∇s, the vector $\omega(\mathbf{x}, \mathbf{y}) \equiv \mathbf{G}(\mathbf{x}, \mathbf{y})\nabla s(\mathbf{y})$ can be represented also by its coordinates $\omega = (\omega_1, \ldots, \omega_d)$ where

$$\omega_i(\mathbf{x}, \mathbf{y}) = \sum_{j=1}^{d} G_{ij}(\mathbf{x}, \mathbf{y})\, \partial_j s(\mathbf{y}). \tag{53}$$

The vector $\omega(\mathbf{x}, \mathbf{y})$ represents the vectorial density of the gradient, because when integrated over the MSC it turns out the value $\nabla s(\mathbf{x})$.

5.2.3. Translational invariance. This is a usual requirement for the laws of Physics, and necessary if the kernel is universal. It implies that there is no preferred place at which objects, events, structures, etc should be expected to be found. In other words, there is no translational bias in the spatial distribution of values. When dealing with experimental signals, which are recorded over bounded domains, the extent of this statistical symmetry is indeed limited although, in general, it is well verified by data. In terms of the integral representation, equation (52), translational invariance implies that the operator density $\mathbf{G}(\mathbf{x}, \mathbf{y})$ does not depend on each variable $\mathbf{x}$ and $\mathbf{y}$ separately, but on its difference $\mathbf{x} - \mathbf{y}$. It follows that

$$\nabla s(\mathbf{x}) = \int_{\mathcal{F}_\infty} \mathrm{d}l(\mathbf{y})\, \mathbf{G}(\mathbf{x} - \mathbf{y})\nabla s(\mathbf{y}). \tag{54}$$

Equation (54) can be simplified to an equivalent scalar form: the left-hand side is a gradient (perhaps in a distributional sense, as signals may present sudden changes as steps). Regarding the gradient as a differential 1-form, it is exact by definition so it must be closed, hence its exterior differential vanishes: $\mathrm{d}\nabla s = 0$. This property is translated to the reconstructor $\mathbf{G}$, in the way

$$\partial_\alpha G_{\beta j}(\mathbf{x}) - \partial_\beta G_{\alpha j}(\mathbf{x}) = 0 \qquad \forall\, \alpha, \beta, j = 1, \ldots, \mathrm{d} \tag{55}$$

that is, the 1-forms $\lambda_j = (G_{1j}, \ldots, G_{dj})$ are all closed for $j = 1, \ldots, d$. As the kernel $\mathcal{G}$ is intended to be universal, it is defined in $\mathbb{R}^d$, which is simply connected. It follows that any closed form in $\mathbb{R}^d$ is exact, from where we conclude that there exists a d-dimensional vector $\mathbf{g} = (g_1, \ldots, g_d)$ such that

$$G_{ij}(\mathbf{x}) = \partial_i g_j(\mathbf{x}) \tag{56}$$

that is, the matrix $\mathbf{G}$ is the gradient of a vector $\mathbf{g}$. We can now simplify equation (54) to obtain

$$s(\mathbf{x}) = \int_{\mathcal{F}_\infty} \mathrm{d}l(\mathbf{y})\, \mathbf{g}(\mathbf{x} - \mathbf{y}) \cdot \nabla s(\mathbf{y}). \tag{57}$$

The equation above can be rewritten in a very useful form by introducing a distributional field which contains all the information which is specific to the signal to be reconstructed. This information is of two types: functional—the values of the gradient ∇s—and geometrical—the MSC. We define the essential gradient of the signal, $\nabla_\infty \mathbf{s}(\mathbf{x})$, as the following distribution

$$\nabla_\infty \mathbf{s}(\mathbf{x}) = \nabla s(\mathbf{x}) \delta_{\mathcal{F}_\infty}(\mathbf{x}) \tag{58}$$

where $\delta_{\mathcal{F}_\infty}(\mathbf{x})$ stands for the density of the proper Hausdorff measure restricted to the set $\mathcal{F}_\infty$ (roughly speaking, a delta function over the connected components defining $\mathcal{F}_\infty$). In this way, equation (57) becomes a standard convolution, as now the integration is performed over all

the space and it is no longer restricted to the MSC. We obtain a practical expression for the reconstruction formula, in the way

$$s(\mathbf{x}) = \int \mathrm{d}\mathbf{y}\, \mathbf{g}(\mathbf{x}-\mathbf{y}) \cdot \nabla_\infty \mathbf{s}(\mathbf{y}) = \mathbf{g} * \nabla_\infty \mathbf{s}(\mathbf{x}) \tag{59}$$

where * stands for the convolution dot-product, see section 2. The reconstruction formula is elegantly expressed in Fourier space as

$$\hat{s}(\mathbf{f}) = \hat{\mathbf{g}}(\mathbf{f}) \cdot \hat{\nabla}_\infty \mathbf{s}(\mathbf{f}) \tag{60}$$

which is an integral equation equivalent to equation (59) and where '·' means the scalar product of the complex vectors. To fully define the reconstruction algorithm, we need to complete the definition of the operator $\mathcal{G}$, now represented by the complex vector field $\hat{\mathbf{g}}(\mathbf{f})$, with the two requirements that we have not yet used.

5.2.4. Isotropy. The functional $\mathcal{G}$ is assumed to be universal, that is, not depending on the specific properties of the signal to be reconstructed: the information on the signal is assumed to be completely represented by the essential gradient $\nabla_\infty \mathbf{s}$. We conclude that the kernel density vector $\mathbf{g}$ is isotropic, that is, it does not possess preferred directions. We can hence decompose it in the following way

$$\hat{\mathbf{g}}(\mathbf{f}) = |\hat{\mathbf{g}}|(\|\mathbf{f}\|)\frac{\sqrt{-1}\mathbf{f}}{\|\mathbf{f}\|} = |\hat{\mathbf{g}}|(\|\mathbf{f}\|)\frac{i\mathbf{f}}{\|\mathbf{f}\|} \tag{61}$$

where $|\hat{\mathbf{g}}|(\|\mathbf{f}\|)$ stands for the modulus of the kernel in the Fourier space. The complex imaginary unit i must be introduced to ensure that the vector $\vec{g}$ is real. Because of the isotropy, $|\hat{\mathbf{g}}|(\|\mathbf{f}\|)$ can only be a function of the modulus $\|\mathbf{f}\|$ of the frequency vector.

5.2.5. Power spectrum. Taking into account that we are dealing with scale invariant systems, it is natural to think that $|\hat{\mathbf{g}}|(\|\mathbf{f}\|)$ is a power law in $\|\mathbf{f}\|$. In fact, to define completely the kernel, we will assume that the power spectrum $S(\|\mathbf{f}\|)$ associated with the ensemble of signals s scales as

$$S(\|\mathbf{f}\|) \sim \frac{1}{\|\mathbf{f}\|^{2-\eta}}, \tag{62}$$

where the deviation exponent η depends on the particularities of the ensemble considered. As we next see, the simplest possible $\hat{\mathbf{g}}$ compatible with this power spectrum is given by $|\hat{\mathbf{g}}|(\|\mathbf{f}\|) = 1/\|\mathbf{f}\|$. Now the definition of the kernel is complete and can be expressed in Fourier space as

$$\hat{\mathbf{g}}(\mathbf{f}) = \frac{i\mathbf{f}}{\|\mathbf{f}\|^2}. \tag{63}$$

Note that, in application of the reconstruction formula, equation (60), the modulus of the Fourier transform of the signal is given by $|\hat{s}(\mathbf{f})| = \mathbf{g}(\|\mathbf{f}\|)A(\mathbf{f})$, where the factor $A(\mathbf{f}) = |\hat{\nabla}_\infty \mathbf{s}(\mathbf{f}) \cdot \|\mathbf{f}\||/\|\mathbf{f}\|$ has a weak dependence on $\|\mathbf{f}\|$ and varies from one signal to another and depends on the particularities of the MSC across the ensemble of signals considered. According to the definition we obtain that the power spectrum is

$$S(\mathbf{f}) = |\hat{\mathbf{g}}|^2(\|\mathbf{f}\|)\,\langle A^2(\mathbf{f})\rangle \tag{64}$$

where the average $\langle\cdot\rangle$ means averaging over the ensemble of signals. Comparing equation (64) with equation (62) we make the assignment of the term $|\mathbf{g}|^2(\|\mathbf{f}\|)$ to the factor $\|\mathbf{f}\|^{-2}$, while the factor $A^2(\mathbf{f})$ introduces the particular anisotropy of the ensemble and would give rise to the weak dependence $\|\mathbf{f}\|^\eta$ in equation (62).

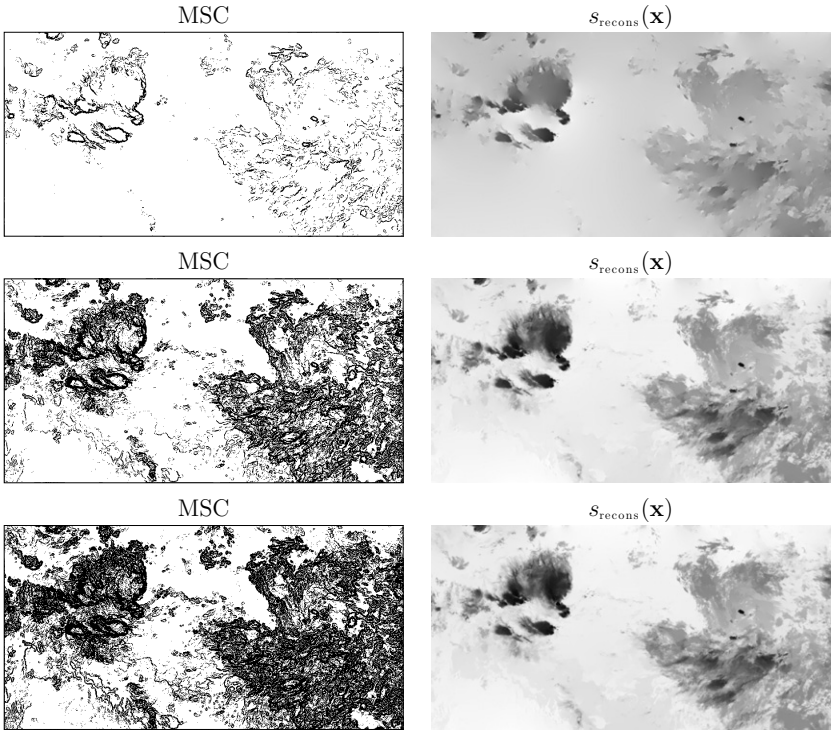

Figure 9. *MeteoSat image*. Results are ordered from top to bottom for changing MSC thresholds: $h_\theta = -0.2$, $h_\theta = 0.0$ and $h_\theta = 0.1$. Left: MSCs; experimental densities: 6.01%, 28.69% and 42.40%. Right: Reconstructions from the MSCs; PSNRs = 20.06 dB, 30.01 dB and 34.91 dB.

We have finally arrived to equation (63), which defines the propagator (indeed equation (59) indicates how to *propagate* the essential gradient away the MSC to restitute the original signal over its whole domain of definition). Substituting this particular expression in equation (60), we obtain the final expression for the reconstruction formula

$$\hat{s}(\mathbf{f}) = \frac{i\mathbf{f} \cdot \hat{\nabla}_\infty \mathbf{s}(\mathbf{f})}{\|\mathbf{f}\|^2}. \tag{65}$$

The reconstruction formula has a very interesting property: no matter the signal considered, equation (65) allows reconstructing the correct $s(\mathbf{x})$ provided that the set $\mathcal{F}_\infty$ (which defines $\nabla_\infty \mathbf{s}$) is large enough: if $\mathcal{F}_\infty$ is taken as the whole signal, $\nabla_\infty \mathbf{s} \equiv \nabla s$ and equation (65) turns out to be a trivial identity. The question is if multifractal signals allow reconstruction considering a rather sparse set $\mathcal{F}_\infty$: the MSC. Experimental results in different types of signal [21, 25, 52, 69, 70] show that the reconstruction formula provides good performance on experimental MSCs, although results can be improved by optimizing the choice of the wavelet [70]. Our proof about the reconstruction algorithm does not prove that such reconstruction exists, but only that if it exists and verifies the required properties, it should take the form expressed in equation (65). So that, while still keeping equation (65), it may happen that the 'minimal' set to allow reconstruction is not the MSC but a different object, 'close' but different to the MSC and hence contributions from other sets should be included. However, a systematic study on the contribution of each singularity component (and also, on the influence of choosing one wavelet or another) was carried out in [70], and the results therein show that the less singular components carry very few or almost no information

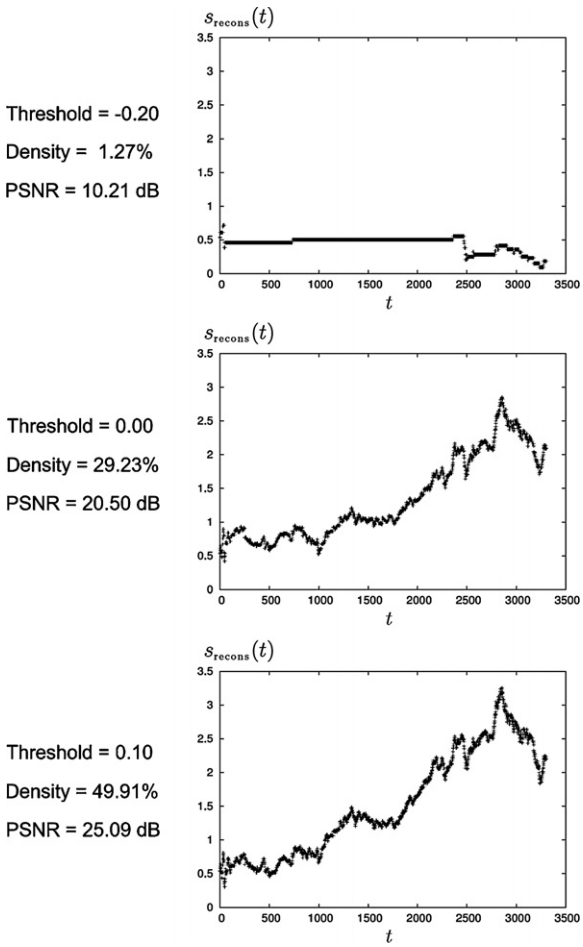

Figure 10. Telefónica^{TM} series. Results are ordered from top to bottom for changing MSC thresholds: $h_\theta = -0.2, h_\theta = 0.0$, and $h_\theta = 0.1$. Left: Summary of results. Right: Reconstructions from the MSCs.

about the scene, mostly randomly distributed and unrelated sets of observable structures. It was concluded that the informative points they may contain are randomly wrongly classified.

5.3. Experimental performance

In the following, we will study the appropriateness and accuracy of the reconstruction formula to describe our chosen example signals. In addition, we will study how the quality of MSC influences the quality of the reconstruction. To measure the quality of a particular reconstructed signal, s_{recons}, we will calculate its dispersion compared to the range of values of the original signal s. We define the error signal as $\epsilon(\mathbf{x}) \equiv s(\mathbf{x}) - s_{\mathrm{recons}}(\mathbf{x})$, and the usual L^2 standard error, σ_{recons}, as

$$\sigma_{\mathrm{recons}} = \left(\frac{1}{\lambda_d(\Omega)} \int_\Omega \mathrm{d}\mathbf{x}\, (s(\mathbf{x}) - s_{\mathrm{recons}}(\mathbf{x}))^2 \right)^{\frac{1}{2}} \tag{66}$$

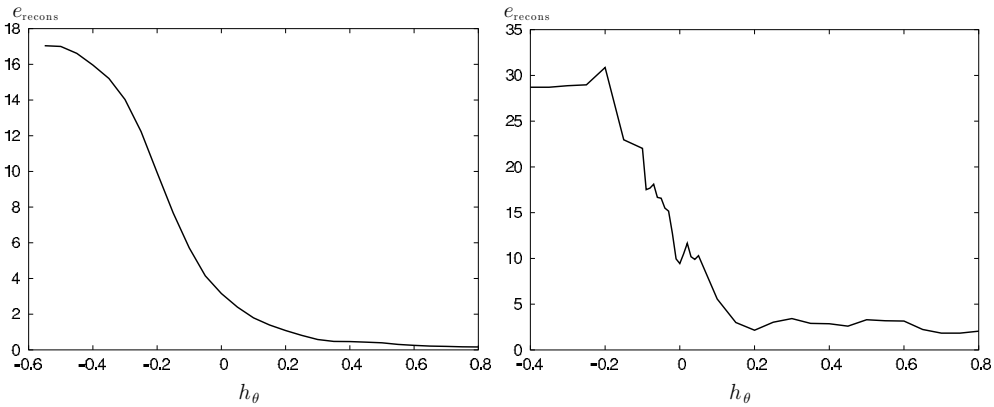

Figure 11. Standard error of the reconstructions from the MSC as a function of the threshold singularity exponent h_θ. Left: MeteoSat image; Right: Telefónica series.

λ_d being the Lebesgue measure on $\mathbb{R}^d$. We will express the error in terms of the relative standard error, e_{recons}, that we define as

$$e_{\text{recons}} \equiv \frac{\sigma_{\text{recons}}}{\Delta_s} \tag{67}$$

where Δ_s is the so-called dynamical range of the signal s, that is, the difference between the maximum and the minimum observed values for s over the compact domain Ω. This quantity is directly related to the peak signal-to-noise ratio (PSNR), which is commonly used in signal engineering: $\text{PSNR} = -20 \log_{10} e_{\text{recons}}$ (for PSNR expressed in decibels, dB). The relative standard error gives us an dimensionless (i.e., without measurement units) measure of the error incurred by a reconstruction. We give here some figures as hints on the significance of the quantity. It is commonly considered that the reconstruction is poor when e_{recons} is greater than 0.10 (PSNR below 20 dB) which corresponds to a situation in which the standard error is above the 10% of the total dynamical range. Reconstructions are considered as remarkable when the relative standard error lies between 0.10 and 0.01 (PSNR from 20 to 40 dB), that is, it represents an amount among 10 and 1% of the dynamical range. Errors below the 1% of the dynamical range (PSNR above 40 dB) can be considered for many applications as perfect reconstructions.

In figures 9 and 10, we present the results of reconstructing the signal with the MSCs (defined as in equation (35)) obtained with different values of singularity threshold h_θ. In all the cases, we evaluate the singularities with the optimized numerical Lorentzian wavelet presented in section 5.3. In figure 9, we show each determination of the MSC and the corresponding reconstruction for the MeteoSat image. In figure 10, we do not represent the different determinations of the MSC because they are difficult to visualize on a 1D plot.

The experimental results presented in the tables show that intermediate values of the singularity threshold h_θ lead to rather sparse determinations of the MSC with good reconstruction quality. We have performed a more detailed study on the quality, computing the evolution of the relative standard error with h_θ. The results are shown in figure 11. In the graphs, it is possible to appreciate that the error diminution is not constant and that it evolves very fast in the region of negative thresholds. An interpretation of this fact could be the following: even if some points fail to be detected as most singular (and thus belonging to the MSC), their estimates have values not far from those of the MSC and hence, as h_θ

increases, they are quickly included in the h_θ-determination of the MSC. In fact let us observe that the MSCs detected for the MeteoSat image are consistently curve-like, that is, they appear as fractals of dimension 1. This is a commonly reported observation in natural images [51, 64], meteorological images [21, 22] and oceanographic images [52]. This one-dimensionality of the MSC is connected to the interpretation of the MSC as a front-like structure. As the value of h_θ increases while still keeping a moderated value, the MSC features a curve-like aspect, which gets coarser and coarser as the value becomes positive. Our results show that values of h_θ around 0 lead to MSCs of moderated density and of good reconstruction quality.

6. Conclusions

In this paper, we have made a review on the theoretical foundations of the microcanonical formulation. The paper revisits some of the key points in this formalism, detailing theoretical and practical aspects in this methodology and extending previous works by providing a coherent, unitary presentation, extended theoretical treatment and numerical implementations.

Microcanonical formalism is based in the assessment of a local structure of singularities, hierarchized in such a way that it gives rise to a multifractal structure. The existence of an actual classification of points, according to the different singularity components composing the system, allows us to extract fine information on the dynamics of the system. In particular, one of the most advantageous features of this formalism is the introduction of reconstructible multifractals, as a natural extension to the microcanonical context of the concept of multiplicative cascade. Reconstructible multifractals are multifractals in the microcanonical sense. Besides, they possess a definite vertex in the multifractal hierarchy, associated with a finite minimum singularity value. The associated singularity component is known as the most singular component (MSC). For reconstructible multifractals, it comprises enough information to fully reconstruct the whole signal just from the gradient restricted to that set. Such a representation of signals has strong implications in terms of dynamical description as well as for coding and compression tasks.

The range of applications of this formalism is wide and far reaching. Future research should be conducted, first, to complete some lacking proofs. Let us recall some of them: the actual existence of a geometrical cascade realizing the multiplicative canonical one, and its consequences for reconstruction. From a technical point of view, research must focus on better implementations of the wavelet singularity analysis. The construction of efficient codes should also be explored. From a theoretical point of view, research should address the need of establishing links in the evolution of multifractals and the known evolution equations (as Navier–Stokes in the case of flows) in order to assess the physical meaning of geometrical entities like the MSC, etc. Lastly, it would be convenient to deduce evolution equations for the canonical representatives of multifractal signals.

Acknowledgments

This work is a contribution to MERSEA (EU AIP3-CT-2003-502885) and OCEANTECH (CSIC PIF-2006) projects. A. Turiel is supported by a Ramón y Cajal contract from the Spanish Ministry of Education and Science. We thank Jordi Isern-Fontanet by his hints and comments during the elaboration of this paper. During this work, H Yahia was granted by INRIA for a 1 year stay at ICM. C J Pérez acknowledges support from MEC under contract FIS2006-13321-C02-01.

Appendix. Scaling requirements for analyzing wavelets over multifractal measures

A.1. General conditions on wavelet tails

In this subsection, we present a qualitative analysis on the influence of the wavelet tail on the value of the exponents. In the next subsection, we will derive a quantitative analysis of that behavior using different assumptions.

We start from the integral form of Lebesgue's density theorem in $\mathbb{R}^d$ [71, vol. 2, 261C]: $\mu_{\|\nabla\|}$-almost everywhere in $\mathbf{x}$, one has

$$\Psi(\mathbf{x}) = \lim_{r\to 0} \frac{1}{\mu_{\|\nabla\|}(B_r(\mathbf{x}))} \int_{B_r(\mathbf{x})} \Psi(\mathbf{y})\, \mathrm{d}\mu_{\|\nabla\|}(\mathbf{y}). \tag{A.1}$$

In the following derivation, we will assume, without loss of generality that $\mathbf{x} = 0$, as the equations are clearer. The wavelet projection of measure $\mu_{\|\nabla\|}$ at $\mathbf{x} = 0$ and at scale r is given by

$$T_\Psi \|\nabla s\|(\mathbf{0}, r) = \frac{1}{r^d} \int_{\mathbf{R}^d} \Psi\left(\frac{\mathbf{y}}{r}\right) \mathrm{d}\mu_{\|\nabla\|}(\mathbf{y}) = \frac{1}{r^d} \int_{\mathbf{R}^d} \Psi_r(\mathbf{y})\, \mathrm{d}\mu_{\|\nabla\|}(\mathbf{y}) \tag{A.2}$$

with

$$\Psi_r(\mathbf{y}) = \Psi\left(\frac{\mathbf{y}}{r}\right). \tag{A.3}$$

Let us denote the sup-norm of $\mathbf{y} \in \mathbf{R}^d$ by $\|\mathbf{y}\|_\infty : \|\mathbf{y}\|_\infty = \sup|y_i|$ with $\mathbf{y} = (y_1, \ldots, y_d)$, and let us decompose the integral in (A.2) in two terms:

$$T_\Psi(\mathbf{0}, r) = \frac{1}{r^d} \int_{\|\mathbf{y}\|_\infty \leqslant y_0} \Psi_r(\mathbf{y})\, \mathrm{d}\mu_{\|\nabla\|}(\mathbf{y}) + \frac{1}{r^d} \int_{\|\mathbf{y}\|_\infty > y_0} \Psi_r(\mathbf{y})\, \mathrm{d}\mu_{\|\nabla\|}(\mathbf{y}) \tag{A.4}$$

with y_0 chosen large enough. The first integral in (A.4) is again split into two terms

$$\frac{1}{r^d} \int_{\|\mathbf{y}\|_\infty \leqslant y_0} \Psi_r(\mathbf{y}) \mathrm{d}\mu_{\|\nabla\|}(\mathbf{y}) = \frac{1}{r^d} \int_{0 \leqslant \|\mathbf{y}\|_\infty \leqslant \alpha} \Psi_r(\mathbf{y})\, \mathrm{d}\mu_{\|\nabla\|}(\mathbf{y}) + \frac{1}{r^d} \int_{\alpha \leqslant \|\mathbf{y}\|_\infty \leqslant y_0} \Psi_r(\mathbf{y})\, \mathrm{d}\mu_{\|\nabla\|}(\mathbf{y}) \tag{A.5}$$

where α will be chosen small enough: $\alpha = r y_0$, with r sufficiently small. In the neighborhood of $\mathbf{0}$, and supposing that Ψ is C^1 around the origin (a reasonable hypothesis for the vast majority of wavelets) we can use the Taylor expansion at first order ($\mathbf{y} = (y_1, \ldots, y_d)$)

$$\Psi_r(\mathbf{y}) = \Psi(\mathbf{0}) + \sum_{i=1}^{d} \frac{y_i}{r} \frac{\partial \Psi}{\partial y_i}(0) + \|\mathbf{y}\| \varepsilon(\mathbf{y}) \tag{A.6}$$

which by substitution into the first integral of equation (A.5) gives

$$\frac{1}{r^d} \int_{0 \leqslant \|\mathbf{y}\|_\infty \leqslant r y_0} \left(\Psi(\mathbf{0}) + \sum_{i=1}^{d} \frac{y_i}{r} \frac{\partial \Psi}{\partial y_i}(0) + \|\mathbf{y}\| \varepsilon(\mathbf{y}) \right) \mathrm{d}\mu_{\|\nabla\|}(\mathbf{y}). \tag{A.7}$$

Then, according to the Lebesgue density theorem (A.1), when $r \to 0$, the integral in (A.7) becomes equivalent to $c\Psi(\mathbf{0}) \frac{1}{r^d} r^{h(\mathbf{0})+d} = c\Psi(\mathbf{0}) r^{h(\mathbf{0})}$ for a suitable constant c. So the first integral in (A.5) lets the singularity exponent at $\mathbf{0}$ unchanged when $r \to 0$, as long as $\Psi(\mathbf{0}) \neq 0$. However, the second integral in (A.5) reveals the 'tail' behavior of the wavelet and it may modify the singularity exponent at $\mathbf{0}$. To see this, let us perform the change of variables

$$\begin{aligned} u_1 &= \Psi\left(\frac{\mathbf{y}}{r}\right) \\ u_2 &= y_2 \\ &\vdots \\ u_d &= y_d \end{aligned} \tag{A.8}$$

in the integral

$$\frac{1}{r^d}\int_{ry_0\leqslant\|\mathbf{y}\|_\infty\leqslant y_0}\Psi_r(\mathbf{y})\,\mathrm{d}\mu_{\|\nabla\|}(\mathbf{y}) \tag{A.9}$$

to get an integral of the form

$$\frac{1}{r^{d-1}}\int_{\substack{\varepsilon_1(r)\leqslant|u_1|\leqslant\gamma\\ u_2,\ldots,u_d}} u_1\|\nabla s\|(r\Psi^{-1}(u_1),u_2,\ldots,u_d)\left|\frac{\partial\Psi^{-1}}{\partial u_1}\right|(\mathbf{u})\,\mathrm{d}\mathbf{u}. \tag{A.10}$$

As Ψ is integrable, the integration domain for variable u_1 between $\varepsilon_1(r)$, which tends to 0 when $r\to 0$, and a fixed γ reflects the decreasing toward 0 of Ψ. If the wavelet Ψ decreases at infinity according to a power law: $\Psi(x)\sim\|\mathbf{x}\|^{-n_0}$ when $\|\mathbf{x}\|\to\infty$, power of n_0 pops up in the integral (A.10) which may change the behavior of $\mu_{\|\nabla\|}$'s singularity exponent at $\mathbf{0}$, when r (and, accordingly, $\varepsilon_1(r)$) tends toward 0.

A.2. Dependence of the retrieved exponents in the asymptotic behavior of the wavelet

In the last subsection, we showed that the tail behavior of the wavelet do influence the values of the singularity exponents. In this subsection, we will derive quantitative information on how the exponents values are perturbed by wavelet's tail. For this purpose, we use a more tractable and different assumption. First, we suppose that we have relations of the form

$$A(\mathbf{x}_0)\,r^{d+h(\mathbf{x}_0)}\leqslant\mu(B_r(\mathbf{x}_0))\leqslant B(\mathbf{x}_0)\,r^{d+h(\mathbf{x}_0)} \tag{A.11}$$

for appropriate positive constants $A(\mathbf{x}_0)$, $B(\mathbf{x}_0)$. The wavelet Ψ will be assumed to be positive to simplify the discussion. In our proof, we will also restrict the discussion to the case of a continuous function Ψ and $\Psi(0)\neq 0$. As will be shown, Ψ will be required to decrease fast enough.

We will assume that for any point $\mathbf{x}$ and any size r the wavelet projection $T_\Psi\mu(\mathbf{x},r)$ is finite. If it was not the case, as μ is σ-finite it would be possible to define a sequence of finite measures μ_n defined over compact supports A_n such that $\mu|_{A_n}=\mu_n$; but Ψ is continuous so the wavelet projections of the μ_n are finite. The proof for μ would be obtained as a limit case, once the theorem is shown to be valid for the μ_n's,

Finally, we will just study the singularity at $\mathbf{x}=0$, the extension for the other points being trivial. We will denote the singularity at $\mathbf{x}=0$ by h_0, in the sense of equation (A.11). The wavelet projections we are interested in are $T_\Psi\mu(0,r)$, given by

$$T_\Psi\mu(\mathbf{0},r)\;=\int\mathrm{d}\mu(\mathbf{x})\,\frac{1}{r^d}\,\Psi\left(\frac{\mathbf{x}}{r}\right). \tag{A.12}$$

The statement of the theorem is as follows:

Theorem A.1. *For any wavelet Ψ belonging to an appropriate class described in the proof, the projection $T_\Psi\mu(\mathbf{0},r)$ satisfies a relation of type (A.11) with exponent $h(\mathbf{0})$*

$$A(\mathbf{0})\,r^{h(\mathbf{0})}\leqslant T_\Psi\mu(\mathbf{0},r)\leqslant B(\mathbf{0})\,r^{h(\mathbf{0})}. \tag{A.13}$$

We will present the proof in three stages, for three different classes of functions: set functions, compact support functions and fast decreasing functions. For the last two types of functions, we will always assume that Ψ is a positive, continuous function and $\Psi(0)\neq 0$ to make the proof simpler.

A.2.1. Set functions. Let $\Psi(\mathbf{x})$ be the set function of the ball of radius $\mathbf{v}$ centered around the origin, that is, $\Psi(\mathbf{x}) = 1_{B_{\mathbf{v}}(\mathbf{0})}(\mathbf{x})$. According to equation (A.12), the wavelet projections of Ψ at $\mathbf{x} = \mathbf{0}$ are given by

$$T_\Psi \mu(\mathbf{0}, r) \;=\; \int \mathrm{d}\mu(\mathbf{x})\, \frac{1}{r^d}\, 1_{B_{\mathbf{v}}(\mathbf{0})}\left(\frac{\mathbf{x}}{r}\right) \;=\; \frac{1}{r^d} \int \mathrm{d}\mu(\mathbf{x})\, 1_{B_{r\mathbf{v}}(0)}\mathbf{x}). \tag{A.14}$$

Hence, it follows

$$T_\Psi \mu(\mathbf{0}, r) \;=\; \frac{1}{r^d} \int_{B_{r\mathbf{v}}(\mathbf{0})} \mathrm{d}\mu(\mathbf{x}) \;=\; \frac{\mu(B_{r\mathbf{v}}(\mathbf{0}))}{r^d} \tag{A.15}$$

so for these simple functions the theorem is trivially verified.

A.2.2. Compact support functions. We will just try to find two constants $0 < A < B$ such that

$$A\, r^{h_0} \;\leqslant\; T_\Psi \mu(\mathbf{0}, r) \;\leqslant\; B\, r^{h_0}. \tag{A.16}$$

A lower bound constant A is easily obtained by the condition of continuity and $\Psi(\mathbf{0}) \neq 0$, as follows: there exists a finite radius $\mathbf{v}$ such that $\Psi(\mathbf{x}) \neq 0\, \forall\, \mathbf{x} \in \mathbf{B}_{\mathbf{v}}(\mathbf{0})$. Let $m > 0$ be the minimum value of $\Psi(\mathbf{x})$ in $\mathbf{B}_{\mathbf{v}}(\mathbf{0})$; then, for all $\mathbf{x}$ the following inequality holds

$$m\; 1_{B_{\mathbf{v}}(\mathbf{0})}(\mathbf{x}) \leqslant \Psi(\mathbf{x}). \tag{A.17}$$

Let $0 < A_0 < B_0$ be the bounding constants for μ at $\mathbf{x} = 0$, that is, such that $A_0 r^{d+h_0} < \mu(B_r(\mathbf{0})) < B_0 r^{d+h_0}$. Then,

$$m\; A_0\; \mathbf{v}^{h_0+d}\; r^{h_0} \leqslant m\; T_{1_{B_{\mathbf{v}}(\mathbf{0})}} \mu(\mathbf{0}, r) \leqslant T_\Psi \mu(\mathbf{0}, r). \tag{A.18}$$

So, A can be taken as $A = m A_0 \mathbf{v}^{h_0+d}$.

To obtain B we will use that Ψ has bounded support; so, there exists a finite radius $\mathbf{w}$ such that $\Psi(x) = 0\, \forall\, \mathbf{x} : \|\mathbf{x}\| > \mathbf{w}$. As Ψ is continuous, it possesses a finite maximum M in $\mathbf{B}_{\mathbf{w}}(\mathbf{0})$. Hence, the following functional inequality holds

$$M\; 1_{\mathbf{B}_{\mathbf{w}}(\mathbf{0})}(\mathbf{x}) \geqslant \Psi(\mathbf{x}). \tag{A.19}$$

and analogously to the case of the lower bound, we conclude that a possible upper bound is given by $B = M B_0 \mathbf{w}^{h_0+d}$.

A.2.3. Fast decreasing functions. We will search constants $0 < A < B$ as in the previous case. The constant A can be calculated exactly like for compact support functions, so we just need to find B.

Let the radius $\mathbf{v}$ be defined as in the previous case and let us define the sets R_i as follows: $R_i \;=\; B_{2^i \mathbf{v}}(\mathbf{0}) - B_{2^{i-1}\mathbf{v}}(\mathbf{0})$ for $i \geqslant 1$ and $R_0 = B_{\mathbf{v}}(0)$. Let M_i be the maximum of Ψ over R_i. Hence, the following functional inequality holds

$$\Phi(\mathbf{x}) = \sum_{i=0}^{\infty} M_i\; 1_{R_i}(\mathbf{x}) \;\geqslant\; \Psi(\mathbf{x}) \tag{A.20}$$

where 1_{R_i} is the set function of R_i, which equals 1 over R_i and 0 outside. We can conclude by proving that there exists an upper bound B for Φ such that $T_\Phi \mu(\mathbf{0}, r) \leqslant B r^{h_0}$, which by equation (A.20) is also an upper bound for Ψ. To obtain this bound, let us suppose that there exists a finite radius $\mathbf{w} > 0$ such that if $\|\mathbf{x}\| > \mathbf{w}$, for all $K > 1$ the function Ψ verifies

$$\Psi(K\mathbf{x}) < \Omega(K)\Psi(\mathbf{x}) \tag{A.21}$$

where $\Omega(K)$ decreases to zero as K goes to infinity faster than any polynomial, that is,

$$\lim_{K\to\infty} K^n \Omega(K) = 0 \qquad \forall n > 0. \tag{A.22}$$

This requirement on Ψ above is a small modification on the condition defining Schwartz's class. We introduce the radius $\mathbf{w}$ to avoid forcing the function to be strictly decreasing from the origin, which would define a very restrictive class of functions. Let i_0 be the least integer greater than $\log_2(\mathbf{w}/\mathbf{v})$. Following equation (A.21), for all $i' > i > i_0$

$$M_{i'} < \Omega(2^{i'-i})\, M_i. \tag{A.23}$$

We will first take r as $r = 2^{-j}$, for $j > 0$ integer. We can thus decompose the dilation of Φ by a factor r, $\Phi(\mathbf{x}/r)$, as

$$\Phi(\mathbf{x}/r) = \sum_{i=0}^{i_0+j} M_i\, 1_{R_i}(\mathbf{x}/r) + \sum_{i=i_0+j+1}^{\infty} M_i\, 1_{R_i}(\mathbf{x}/r) = \Phi_j(\mathbf{x}) + \delta_j(\mathbf{x}). \tag{A.24}$$

For $i > i_0 + j$, $1_{R_i}(\mathbf{x}/r) = 1_{R_i}(2^j\mathbf{x}) = 1_{R_{i-j}}(\mathbf{x})$. The residual function $\delta_j(\mathbf{x})$ verifies the following bound (obtained applying equation (A.23)):

$$\delta_j(\mathbf{x}) < \Omega(1/r) \sum_{i=i_0}^{\infty} M_i\, 1_{R_i}(\mathbf{x}) = \Omega(1/r)\, \delta_0(\mathbf{x}). \tag{A.25}$$

Given the dependence of $\delta_j(\mathbf{x})$ in r, it decays very fast, and this function is negligible in comparison with any power of r, so we can ignore this part. Hence, $T_\Phi\mu(\mathbf{0}, r) \approx T_{\Phi_j}\mu(\mathbf{0}, r)$ for $r = 2^{-j}$. For a general value of r, we also obtain $T_\Phi\mu(\mathbf{0}, r) \approx T_{\Phi_j}\mu(\mathbf{0}, r)$ where j is such that $2^{-j-1} < r \leqslant 2^{-j}$. Taking into account that

$$T_{1_{R_i}}\mu(\mathbf{0}, r) \leqslant \mathbf{v}^{h_0+d}\, 2^{(h_0+d)i}\, (B_0 - 2^{-(h_0+d)}\, A_0)\, r^{h_0} \tag{A.26}$$

it follows

$$T_{\Phi_j}\mu(\mathbf{0}, r) \leqslant \mathbf{v}^{h_0+d}\, (B_0 - 2^{-(h_0+d)}\, A_0) \left(\sum_{i=0}^{i_0+j} 2^{(h_0+d)i}\, M_i \right) r^{h_0} \tag{A.27}$$

so the upper bound B is given by

$$B = \mathbf{v}^{h_0+d}\, (B_0 - 2^{-(h_0+d)}\, A_0) \sum_{i=0}^{\infty} 2^{(h_0+d)i}\, M_i \tag{A.28}$$

where the series $\sum_{i=0}^{\infty} 2^{(h_0+d)i}\, M_i$ is finite due to the fast decreasing of M_i.

A.2.4. Refined choices for the wavelet. The previous section gives a proof of the capability as singularity analyzers for wavelets Ψ chosen in a very restrictive class of functions. Some of the conditions can be relaxed from a mathematical point of view (for instance, the requirement of continuity could be relaxed to integrability and boundness), although their precise formulation does not change very much the result in practical applications. It is also clear that singularities can be detected just using positive wavelets, but non-positive wavelets could be used as well. So none of those conditions is going to change significantly the main result nor the experimental performance (except for the questions already discussed concerning the minimum distinguishable resolution). However, there is a requirement which is critical to extract singularities and whose correct tuning allows us to improve significantly the performance; namely, the condition of fast decay expressed in equation (A.22).

Any *a priori* knowledge about the properties of the multifractal measure μ allows enlarging the class of valid wavelets by relaxing the fast decay condition. The most relevant information

is the knowledge of bounds on the range of possible singularity exponents h_0. Let us assume that there exists a maximum singularity exponent h_m. In this case, the fast decay condition can be modified so that equation (A.22) is only required for $n \leqslant n_0 \equiv d + h_m$. The argument goes as follows: let us assume that for $\|\mathbf{x}\|$ large enough, $|\Psi(\mathbf{x})| \sim \|\mathbf{x}\|^{-n_0}$ (in the sense that $\lim_{\|\mathbf{x}\|\to\infty} \|\mathbf{x}\|^{n_0}\|\Psi(\mathbf{x})\|$ is not divergent). So, $\Omega(\|\mathbf{x}\|) \propto \|\mathbf{x}\|^{-n_0}$ and M_i is then given by $M_i \propto 2^{-n_0 i}$. The existence of the upper bound B given in equation (A.28) is limited to the cases in which the series appearing in the definition is finite but for the wavelet we consider now this series is proportional to

$$\sum_{i=0}^{\infty} 2^{(h_0+d-n_0)i} \tag{A.29}$$

which converges if $n_0 > h_0 + d$ and diverges for $n_0 \leqslant h_0 + d$. So, it suffices to take $n_0 > h_m + d$ to assure the convergence; otherwise, the definition of B above does not hold; in fact, in that case $T_{\Phi_j}\mu(\mathbf{0}, r)$ is trivially dominated by a factor r^{n_0-d} directly coming from the asymptotic behavior of Ψ. This allows us to refine the proof above as follows: let $\Psi(\mathbf{x})$ a wavelet decaying as $\|\mathbf{x}\|^{-n_0}$ at the infinity. Then, at any point $\mathbf{x}$ in which $\mu(B_r(\mathbf{x})) \sim \alpha(\mathbf{x})\, r^{h(\mathbf{x})+d}$, the wavelet projection is given by $T_\Psi\mu(\mathbf{x}, r) \sim r^{h_\Psi(\mathbf{x})}$, where

$$h_\Psi(\mathbf{x}) = \begin{cases} h(\mathbf{x}), & h(\mathbf{x}) < n_0 - d \\ n_0 - d, & h(\mathbf{x}) \geqslant n_0 - d. \end{cases} \tag{A.30}$$

References

[1] Green M S, Domb C and Lebowitz J L 1972 *Phase Transitions and Critical Phenomena* (New York: Academic)

[2] Stanley H E 1987 *Introduction to Phase Transitions and Critical Phenomena* (Oxford, UK: Oxford Science Publications)

[3] Uzunov D I 1992 *Introduction to the Theory of Critical Phenomena* (Singapore: World Scientific)

[4] Fisher A J, Binney J J, Dowrick N J and Newman M E J 1992 *The Theory of Critical Phenomena. An Introduction to Renormalization Group* (Oxford: Clarendon)

[5] Falconer K 1990 *Fractal Geometry: Mathematical Foundations and Applications* (Chichester: Wiley)

[6] Parisi G and Frisch U 1985 On the singularity structure of fully developed turbulence *Turbulence and Predictability in Geophysical Fluid Dynamics: Proc. Intl School of Physics E. Fermi* ed M Ghil, R Benzi and G Parisi (Amsterdam: North-Holland) pp 84–7

[7] Halsey T C, Jensen M H, Kadanoff L P, Procaccia I and Shraiman I 1986 Fractal measures and their singularities: the characterization of strange sets *Phys. Rev.* A **33** 1141–51

[8] Arneodo A, Argoul F, Bacry E, Elezgaray J and Muzy J F 1995 *Ondelettes, Multifractales et Turbulence* (Paris, France: Diderot Editeur)

[9] Crouse M S, Nowak R D and Baraniuk R G 1998 Wavelet-based statistical signal processing using hidden Markov models *IEEE Trans. Signal Process.* **46** 886–902

[10] Ruderman D L and Bialek W 1994 Statistics of natural images: scaling in the woods *Phys. Rev. Lett.* **73** 814

[11] Arimitsu T and Arimitsu N 2002 Analysis of velocity fluctuation in turbulence based on generalized statistics *J. Phys.: Condens. Matter* **14** 2237–46

[12] Frisch U 1995 *Turbulence* (Cambridge: Cambridge University Press)

[13] Tollhurst D J, Tadmor Y and Tang Ch 1992 Amplitude spectra of natural images *Ophthalm. Physiol. Opt.* **12** 229–32

[14] Ruderman D L 1994 Designing receptive fields for highest fidelity *Network* **5** 147–56

[15] Liu Y, Gopikrishnan P, Cizeau P, Meyer M, Peng C-K and Stanley H E 1999 The statistical properties of the volatility of price fluctuations *Phys. Rev.* E **60** 1390–400

[16] Davis A, Marshak A and Wiscombe W 1994 Wavelet based multifractal analysis of non-stationary and/or intermittent geophysical signals *Wavelets in Geophysics* ed E Foufoula-Georgiou and P Kumar (New York: Academic) pp 249–98

[17] Gopikrishnan P, Plerou V, Liu Y, Amaral L A N, Gabaix X and Stanley H E 2000 Scaling and correlation in financial time series *Physica* A **287** 362–73

[18] Peng C-K, Buldyrev S V, Goldberger A L, Havlin S, Sciortino F, Simons M and Stanley H E 1992 Long-range correlations in nucleotide sequences *Nature* **356** 168–70
[19] Daubechies I 1992 *Ten Lectures on Wavelets (CBMS-NSF Series in Appl. Math.)* (Montpelier, Vermont: Capital City Press)
[20] Mallat S 1999 *A Wavelet Tour of Signal Processing* 2nd edn (New York: Academic)
[21] Turiel A, Grazzini J and Yahia H 2005 Multiscale techniques for the detection of precipitation using thermal IR satellite images *IEEE Geosci. Remote Sens. Lett.* **2** 447–50
[22] Grazzini J, Turiel A and Yahia H 2002 Entropy estimation and multiscale processing in meteorological satellite images *Proc. ICPR 2002 (Los Alamitos, CA)* vol 3 (Los Alamitos, CA: IEEE Computer Society) pp 764–8
[23] Mandelbrot B B, Fisher A and Calvet L 1997 A multifractal model of asset returns *Cowles Foundation Discussion Paper No. 1164*
[24] Muzy J F, Delour J and Bacry E 2000 Modelling fluctuations of financial time series: from cascade process to stochastic volatility model *Euro. Phys. J.* B **17** 537–48
[25] Turiel A and Pérez-Vicente C 2003 Multifractal geometry in stock market time series *Physica* A **322** 629–49
[26] Muzy J F, Bacry E and Arneodo A 1991 Wavelets and multifractal formalism for singular signals: application to turbulence data *Phys. Rev. Lett.* **67** 3515–8
[27] Benzi R, Biferale L, Crisanti A, Paladin G, Vergassola M and Vulpiani A 1993 A random process for the construction of multiaffine fields *Physica* D **65** 352–8
[28] Benzi R, Ciliberto S, Baudet C, Ruiz Chavarria G and Tripiccione C 1993 Extended self similarity in the dissipation range of fully developed turbulence *Europhys. Lett.* **24** 275–9
[29] Bacry E, Muzy J F and Arneodo A 1993 Singularity spectrum of fractal signals from wavelet analysis: exact results *J. Stat. Phys.* **70** 635–73
[30] Jaffard S 1997 Multifractal formalism for functions: I. Results valid for all functions *SIAM J. Math. Anal.* **28** 944–70
[31] Benzi R, Paladin G, Parisi G and Vulpiani A 1984 On the multifractal nature of fully developed turbulence and chaotic systems *J. Phys. A: Math. Gen.* **17** 3521–31
[32] Meneveau C and Sreenivasan K R 1987 Simple multifractal cascade model for fully developed turbulence *Phys. Rev. Lett.* **59** 1424–7 (10.1103/PhysRevLett.59.1424)
[33] Arrault J, Arneodo A, Davis A and Marshak A 1997 Wavelet-based multifractal analysis of rough surfaces: application to cloud models and satellite data *Phys. Rev. Lett.* **79** 75–9
[34] Roux S G, Arneodo A and Decoster N 2000 A wavelet-based method for multifractal image analysis: III. Applications to high-resolution satellite images of cloud structure *Eur. Phys. J.* B **15** 765–86
[35] Mandelbrot B B 1991 Random multifractals: negative dimensions and the resulting limitations of the thermodynamic formalism *Proc. R. Soc.* A **434** 79–88
[36] Turiel A, Mato G, Parga N and Nadal J P 1998 The self-similarity properties of natural images resemble those of turbulent flows *Phys. Rev. Lett.* **80** 1098–101
[37] Nevado A, Turiel A and Parga N 2000 Scene dependence of the non-Gaussian scaling properties of natural images *Network* **11** 131–52
[38] Amaral L A N, Goldberger A L, Ivanov P Ch and Stanley H E 1998 Scale-independent measures and pathologic cardiac dynamics *Phys. Rev. Lett.* **81** 2388–91
[39] Ivanov P, Amaral L, Goldberger A, Havlin S, Rosenblum M, Struzik Z and Stanley H 1999 Multifractality in human heartbeat dynamics *Nature* **399** 461–5
[40] Arneodo A *et al* 1996 Structure functions in turbulence, in various flow configurations, at Reynolds number between 30 and 5000, using extended self-similarity *Europhys. Lett.* **34** 411–6
[41] Kolmogorov A N 1941 Dissipation of energy in a locally isotropic turbulence *Dokl. Akad. Nauk. SSSR* **32** 141
[42] Turiel A and Parga N 2000 Multifractal wavelet filter of natural images *Phys. Rev. Lett.* **85** 3325–8
[43] Turiel A, Nadal J-P and Parga N 2003 Orientational minimal redundancy wavelets: from edge detection to perception *Vis. Res.* **43** 1061–79
[44] Rudin W 1987 *Real and Complex Analysis* (New York: McGraw-Hill)
[45] Derrida B 1981 Random energy model: an exactly solvable model of disordered systems *Phys. Rev.* B **24** 2613–26
[46] Carleman T 1922 Sur le problème des moments *C. R. Acad. Sci., Paris* **174** 1680
[47] Novikov E A 1994 Infinitely divisible distributions in turbulence *Phys. Rev.* E **50** R3303
[48] Gupta V K and Waymire E C 1993 A statistical analysis of mesoscale rainfall as a random cascade *J. Appl. Meteorol.* **32** 251–67
[49] Schertzer D, Lovejoy S and Hubert P 2002 An introduction to stochastic multifractal fields *ISFMA Symp. on Enviornmental Sciences and Engineering with Related Mathematical Problems* ed A Ern and W Liu (Beijing: High Education Press)

[50] Schertzer D and Lovejoy S 1997 Universal multifractals do exist!: comments on 'a statistical analysis of mesoscale rainfall as a random cascade' *J. Appl. Meteorol.* **36** 1296–303
[51] Turiel A and Parga N 2000 The multi-fractal structure of contrast changes in natural images: from sharp edges to textures *Neural Comput.* **12** 763–93
[52] Turiel A, Isern-Fontanet J, García-Ladona E and Font J 2005 Multifractal method for the instantaneous evaluation of the stream function in geophysical flows *Phys. Rev. Lett.* **95** 104502
[53] Turiel A, Pérez-Vicente C and Grazzini J 2006 Numerical methods for the estimation of multifractal singularity spectra on sampled data: a comparative study *J. Comput. Phys.* **216** 362–90
[54] Pont O, Turiel A and Perez-Vicente C J 2006 Application of the microcanonical multifractal formalism to monofractal systems *Phys. Rev.* E **74** 061110
[55] Chhabra A B, Meneveau C, Jensen R V and Sreenivasan K R 1989 Direct determination of the f(*alpha*) singularity spectrum and its application to fully developed turbulence *Phys. Rev.* A **40** 5284–94
[56] Sreenivasan K R 1991 Fractals and multifractals in fluid turbulence *Ann. Rev. Fluid. Mech.* **23** 539–600
[57] Arneodo A 1996 Wavelet analysis of fractals: from the mathematical concepts to experimental reality *Wavelets. Theory and Applications (ICASE/LaRC Series in Computational Science and Engineering)* ed G Erlebacher, M Yousuff Hussaini and L M Jameson (Oxford: Oxford University Press) p 349
[58] Struzik Z R 2000 Determining local singularity strengths and their spectra with the wavelet transform *Fractals* **8** 163–79
[59] Tchiguirinsakaia I, Schertzer D, Lovejoy S, Hubert P and Bendjoudi H 2004 Techniques multifractales et gestion du cycle de l'eau *Proc. Journées d'étude sur les méthodes pour les signaux complexes en traitement d'image (Rocquencourt, INRIA)* ed J-P Nadal, A Turiel and H Yahia pp 67–75
[60] Arneodo A, Bacry E, Jaffard S and Muzy J F 1997 Oscillating singularities on cantor sets. a grand canonical multifractal formalism *J. Stat. Phys.* **87** 179–209
[61] Arneodo A, Bacry E, Jaffard S and Muzy J F 1998 Singularity spectrum of multifractal functions involving oscillating singularities *J. Fourier Anal. Appl.* **4** 159–74
[62] Mallat S and Zhong S 1991 Wavelet transform maxima and multiscale edges *Wavelets and Their Applications* ed M B Ruskai (Boston: Jones and Bartlett)
[63] Kestener P and Arnéodo A *et al* 2003 Three-dimensional wavelet-based multifractal method: the need for revisiting the multifractal description of turbulence dissipation data *Phys. Rev. Lett.* **91** 194501
[64] Turiel A, Parga N, Ruderman D and Cronin T 2000 Multiscaling and information content of natural color images *Phys. Rev.* E **62** 1138–48
[65] She Z S and Leveque E 1994 Universal scaling laws in fully developed turbulence *Phys. Rev. Lett.* **72** 336–9
[66] Dubrulle B 1994 Intermittency in fully developed turbulence: log-Poisson statistics and generalized scale covariance *Phys. Rev. Lett.* **73** 959–62
[67] She Z S and Waymire E C 1995 Quantized energy cascade and log-Poisson statistics in fully developed turbulence *Phys. Rev. Lett.* **74** 262–5
[68] Castaing B 1996 The temperature of turbulent flows *J. Phys.* II **6** 105–14
[69] Turiel A and del Pozo A 2002 Reconstructing images from their most singular fractal manifold *IEEE Trans. Image Process.* **11** 345–50
[70] Turiel A 2003 Relevance of multifractal textures in static images *Electron. Lett. Comput. Vis. Image Anal.* **1** 35–49
[71] Fremlin D H 2001 *Measure Theory, volumes 1–5.* Torres Fremlin. Also available on-line at http://www.essex.ac.uk/maths/staff/fremlin/mt.htm., Torres Fremlin, 25 Ireton Road, Colchester, CO3 3AT, England